Electronic Supplementary Material (ESI) for Physical Chemistry Chemical Physics.

Supporting Information:

A computational study of the vibronic spectroscopy and photophysics of aza[7]helicene

Yanli Liu,[*,†] Daniel Aranda,[*,‡] and Fabrizio Santoro[*,‡]

†*School of Physics and Optoelectronics Engineering, Ludong University, 264025 Yantai, Shandong, PR China*

‡*CNR–Consiglio Nazionale delle Ricerche, Istituto di Chimica dei Composti Organo Metallici (ICCOM-CNR), SS di Pisa, Area della Ricerca, via G. Moruzzi 1, I-56124 Pisa, Italy*

E-mail: yanliliu@ldu.edu.cn; daniel.aranda@pi.iccom.cnr.it; fabrizio.santoro@pi.iccom.cnr.it

Contents

S1 Theory

S1.1 The ABS and ECD spectra

S1.1.1 Time-dependent expression for the ABS and ECD spectra

The ABS spectrum at T=0K in a sum over states time-independent formalism includes the contribution from all the transitions from the vibrational ground state $|\mathbf{0}\rangle$ of the electronic ground state $|g\rangle$ (with energy $E_0 = \hbar\omega_0$) to all the vibronic eigenstates $|f\rangle$ ($E = \hbar\omega_f$), and can be expressed as

$$\epsilon(\omega) = \frac{4\pi^2 \times \omega \times N_A}{3000 \times \ln 10 \times \hbar c_0 \times (4\pi\epsilon_0)} \times \sum_f F(\omega)\langle \mathbf{0}; g|\boldsymbol{\mu}|f\rangle\langle f|\boldsymbol{\mu}|g; \mathbf{0}\rangle \delta(\omega + \omega_0 - \omega_f) \quad (1)$$

Where $F(\omega)$ is a broadening function. Similarly, the ECD spectrum in terms of the anisotropy of the molar absorptivity $\Delta\epsilon(\omega) = \epsilon_L - \epsilon_R$ is

$$\Delta\epsilon(\omega) = \frac{16\pi^2 \times \omega \times N_A}{3000 \times \ln 10 \times \hbar c_0^2 \times (4\pi\epsilon_0)} \sum_f F(\omega) Im\left[\langle \mathbf{0}; g|\boldsymbol{\mu}|f\rangle\langle f|\boldsymbol{m}|g; \mathbf{0}\rangle\right] \delta(\omega + \omega_0 - \omega_f) \quad (2)$$

where $\boldsymbol{\mu}$ and $\mathbf{m}$ are the electric and magnetic transition dipole moments, respectively, and ϵ_0 and c_0 represents the the electric vacuum permittivity and speed of light in vacuum. In Franck-Condon (FC) approximation the transitions dipole moments can be written in spectral form as follows:

$$\boldsymbol{\mu} = \sum_i \left(\boldsymbol{\mu}_{gi}|g\rangle\langle d_i| + \boldsymbol{\mu}_{ig}|d_i\rangle\langle g|\right). \quad (3)$$

$$\boldsymbol{m} = \sum_i \left(\boldsymbol{m}_{gi}|g\rangle\langle d_i| + \boldsymbol{m}_{ig}|d_i\rangle\langle g|\right). \quad (4)$$

with d_i as the diabatic states. For brevity sake, we simply use $\mathbf{m}$ to represent its imaginary part.

Expressing the delta function in the time domain, and combining the physical constants in one, we have

$$\delta(\omega + \omega_0 - \omega_f) = \frac{1}{2\pi} \int_{-\infty}^{\infty} dt e^{i(\omega+\omega_0-\omega_f)t}, \tag{5}$$

$$\mathcal{C}_\epsilon = \frac{2\pi \times N_A}{3000 \times \ln 10 \times \hbar c_0 \times (4\pi\epsilon_0)} \tag{6}$$

$$\mathcal{C}_{\Delta\epsilon} = \frac{8\pi \times N_A}{3000 \times \ln 10 \times \hbar c_0^2 \times (4\pi\epsilon_0)} \tag{7}$$

The time-independent Eqs. 1 and 2 can be transformed into time-dependent expressions, suitable for computation through wavepacket dynamics.

$$\epsilon(\omega) = \mathcal{C}_\epsilon \omega \sum_f \int_{-\infty}^{\infty} dt F(t) e^{i(\omega+\omega_0)t} \langle \mathbf{0}; g|\boldsymbol{\mu}|f\rangle e^{-i\omega_f t} \langle f|\boldsymbol{\mu}|g; \mathbf{0}\rangle \tag{8}$$

$$\Delta\epsilon(\omega) = \mathcal{C}_{\Delta\epsilon} \omega \sum_f \int_{-\infty}^{\infty} dt F(t) e^{i(\omega+\omega_0)t} \langle \mathbf{0}; g|\boldsymbol{\mu}|f\rangle e^{-i\omega_f t} \langle f|\boldsymbol{m}|g; \mathbf{0}\rangle \tag{9}$$

Notice that the broadening function in frequency $F(\omega)$ becomes a damping function in time $F(t)$. Substituting $\sum_f |f\rangle e^{-i\omega_f t}\langle f| = e^{-i\hat{H}t/\hbar}$ and expanding the transition dipoles according to Eqs. 3 and 4, we obtain for the case of diabatic states d

$$
\begin{aligned}
\epsilon(\omega) &= \mathcal{C}_\epsilon \omega \sum_{ji} \int_{-\infty}^{\infty} dt F(t) e^{i(\omega+\omega_0)t} \langle \mathbf{0}; d_j | \boldsymbol{\mu}_{gj} e^{-i\hat{H}t/\hbar} \boldsymbol{\mu}_{ig} | d_i; \mathbf{0} \rangle \\
&= \sum_{ii} \epsilon_{ii}(\omega) + \sum_{ij, j\neq i} \epsilon_{ij}(\omega) = \epsilon^{auto}(\omega) + \epsilon^{cross}(\omega) \qquad (10) \\
\Delta\epsilon(\omega) &= \mathcal{C}_{\Delta\epsilon} \omega \sum_{ji} \int_{-\infty}^{\infty} dt F(t) e^{i(\omega+\omega_0)t} \langle \mathbf{0}; d_j | \boldsymbol{\mu}_{gj} e^{-i\hat{H}t/\hbar} \mathbf{m}_{ig} | d_i; \mathbf{0} \rangle \\
&= \sum_{ii} \Delta\epsilon_{ii}(\omega) + \sum_{ij, j\neq i} \Delta\epsilon_{ij}(\omega) \\
&= \Delta\epsilon^{auto}(\omega) + \Delta\epsilon^{cross}(\omega) \qquad (11)
\end{aligned}
$$

S1.1.2 Total Intensities

By setting a Gaussian broadening function and inserting into the correlation function of Eqs. 1 and 2 a resolution of the identity in eigenstate basis $\sum_\beta |\beta\rangle\langle\beta| = 1$ and using $e^{-i\hat{H}t/\hbar}|\beta\rangle = e^{-iE_\beta t/\hbar}|\beta\rangle$, the total intensities can be obtained from the lineshapes $\epsilon(\omega)/\omega$ and $\Delta\epsilon(\omega)/\omega$ (see Ref. [S1]). Neglecting the prefactors $\mathcal{C}_\epsilon$ and $\mathcal{C}_{\Delta\epsilon}$ it yields:

$$
\begin{aligned}
I_{ABS} &= \sum_{ji,\beta} \langle \mathbf{0}; d_j | \boldsymbol{\mu}_{gj} | \beta \rangle \langle \beta | \boldsymbol{\mu}_{ig} | d_i; \mathbf{0} \rangle \qquad (12) \\
I_{ECD} &= \sum_{ji\beta} \langle \mathbf{0}; d_j | \boldsymbol{m}_{gj} | \beta \rangle \langle \beta | \boldsymbol{\mu}_{ig} | d_i; \mathbf{0} \rangle \qquad (13)
\end{aligned}
$$

Removing the identity over eigenstates β

$$I_{ABS} = \sum_{ij} \langle d_j | d_i \rangle \langle \mathbf{0} | \boldsymbol{\mu}_{gj} \boldsymbol{\mu}_{ig} | \mathbf{0} \rangle \tag{14}$$

$$I_{ECD} = \sum_{ij} \langle d_j | d_i \rangle \langle \mathbf{0} | \boldsymbol{m}_{gj} \boldsymbol{\mu}_{ig} | \mathbf{0} \rangle \tag{15}$$

Because the reference diabatic states are orthogonal, only the diagonal terms contribute to the total intensity and we finally get

$$I_{ABS} = \sum_{i} \langle \mathbf{0} | \boldsymbol{\mu}_{gi} \boldsymbol{\mu}_{ig} | \mathbf{0} \rangle \tag{16}$$

$$I_{ECD} = \sum_{i} \langle \mathbf{0} | \boldsymbol{m}_{gi} \boldsymbol{\mu}_{ig} | \mathbf{0} \rangle \tag{17}$$

Taking advantage of the coordinate independence of the transition dipole moments of diabatic states, as implicit in the LVC model, the transitions dipoles can be extracted from the brackets, which simply gives

$$I_{ABS}^{LVC} = \sum_{i} |\boldsymbol{\mu}_{gi}^{FC}|^2 = \sum_{i} D_{gi}^{FC} \tag{18}$$

$$I_{ECD}^{LVC} = \sum_{i} \boldsymbol{m}_{gi}^{FC} \boldsymbol{\mu}_{ig}^{FC} = \sum_{i} R_{gi}^{FC} \tag{19}$$

Therefore, the total absorption and ECD intensities are equal to the sum of the dipole or rotatory strengths of the $|g\rangle \rightarrow |i\rangle$ excited states, which coincides with what expected for an adiabatic FC|VG calculation, therefore

$$I_{ABS}^{FC} = I_{ABS}^{LVC} = \sum_i |\boldsymbol{\mu}_{gi}^{FC}|^2 = \sum_i D_{gi}^{FC} \quad (20)$$

$$I_{ECD}^{FC} = I_{ECD}^{LVC} = \sum_i \boldsymbol{m}_{gi}^{FC} \boldsymbol{\mu}_{ig}^{FC} = \sum_i R_{gi}^{FC} \quad (21)$$

For an adiabatic FCHT calculation the linear term of the transition dipoles must be included. The integrals can be calculated using second quantization $q_\alpha = 1/\sqrt{2}(a_\alpha + a_\alpha^+)$ obtaining

$$I_{ABS}^{FCHT} = I_{ABS}^{FC} + \frac{1}{2}\sum_{i\alpha}\left[\left(\frac{\partial \boldsymbol{\mu}_{gi}^{ad,LVC}(\mathbf{q})}{\partial q_\alpha}\right)_{FC}\right]^2 = \sum_i \left(I_{ABS,i}^{FC} + I_{ABS,i}^{HT}\right) \quad (22)$$

$$\begin{aligned} I_{ECD}^{FCHT} &= I_{ECD}^{FC} + \frac{1}{2}\sum_{i\alpha}\left(\frac{\partial \boldsymbol{m}_{gi}^{ad,LVC}(\mathbf{q})}{\partial q_\alpha}\right)_{FC}\left(\frac{\partial \boldsymbol{\mu}_{ig}^{ad,LVC}(\mathbf{q})}{\partial q_\alpha}\right)_{FC} \\ &= \sum_i \left(I_{ECD,i}^{FC} + I_{ECD,i}^{HT}\right) \end{aligned} \quad (23)$$

Notice that at FCHT level the total intensity has a second term (HT) to add to the FC and LVC one and that depends on the transition dipoles derivatives. For ABS it is always positive and $I_{ABS}^{FCHT} > I_{ABS}^{FC}$ by definition. For ECD, HT contribution of each mode can have different signs, so that HT contribution to the total intensity can be very small even they have strong HT effects because of mutual cancellations. In this case, the sum of the absolute values ($\mathrm{R}_{tot}^{|HT|}$) can be useful:

$$I_{ECD}^{|HT|} = \frac{1}{2}\sum_{i\alpha}\left|\left(\frac{\partial \boldsymbol{m}_{gi}^{ad,LVC}(\mathbf{q})}{\partial q_\alpha}\right)_{FC}\left(\frac{\partial \boldsymbol{\mu}_{ig}^{ad,LVC}(\mathbf{q})}{\partial q_\alpha}\right)_{FC}\right| \tag{24}$$

S1.2 Parameterization of the LVC model

The adiabatic states calculated on the ground state structure are taken as reference diabatic states. Then, the molecular structure is distorted along each normal mode q_α by a small quantity $\pm\Delta_\alpha$ and the diabatic states are defined as the combination of adiabatic states most similar to the reference states. Therefore, the transformation between diabatic $|\mathbf{d}^{(r)}\rangle$ and adiabatic $|\mathbf{a}^{(r)}(\Delta_\alpha)\rangle$ states is:

$$|\mathbf{d}^{(r)}\rangle = |\mathbf{a}^{(r)}(\Delta_\alpha)\rangle\mathbf{D}(\Delta_\alpha) \tag{25}$$

where the elements of the matrix $\mathbf{D}$ are $D_{ji}(\Delta_\alpha) = \langle a_j(\Delta_\alpha)|d_i\rangle$. This transformation allows us to obtain the diabatic potential energies from the adiabatic by applying:

$$\mathbf{V}^{dia}(\Delta_\alpha) = \mathbf{D}^T(\Delta_\alpha)\mathbf{V}^{ad}(\Delta_\alpha)\mathbf{D}(\Delta_\alpha) \tag{26}$$

Once the diabatic potential energies are known, the LVC parameters, i.e. the interstate couplings for each normal coordinate and pair of states $\lambda_{ij}(\alpha)$, are computed by numerical differentiation for both the cases $i = j$ and $i \neq j$ as

$$\lambda_{ij}(\alpha) = \frac{\partial V_{ij}^{dia}(\mathbf{q})}{\partial q_\alpha} \simeq \frac{V_{ij}^{dia}(\Delta_\alpha) - V_{ij}^{dia}(-\Delta_\alpha)}{2\Delta_\alpha} \tag{27}$$

To find the transformation matrix $\mathbf{D}$ we use a method very similar to what pro-

posed by Neugebauer for TD-DFT,[S2] and previously reported for Configuration-Interaction wave functions by Cimiraglia et al.[S3] The matrix $\mathbf{D}$ is found to be:

$$\mathbf{D} = \mathbf{S}^T(\mathbf{S}\mathbf{S}^T)^{-\frac{1}{2}}. \tag{28}$$

where $\mathbf{S}$ is the matrix of the overlaps between reference and displaced adiabatic states (see Yaghoubi et al.[S4] for the full description).

S1.3 Adiabatic states from the LVC model: transition dipole derivatives and nonadiabatic couplings

Similarly to what presented in the previous section, it is possible to obtain the adiabatic states from diagonalization of the diabatic potential energy matrix $V^{dia}(\mathbf{q})$. This requires the transformation

$$|\mathbf{a}^{(r,LVC)}(\mathbf{q})\rangle = |\mathbf{d}^{(r)}\rangle\, \mathbf{U}(\mathbf{q}) \tag{29}$$

where $\mathbf{U}(\mathbf{q})$ is the matrix of the eigenvectors, and the energies of the states is obtained from the diagonal elements $\mathbf{E}^{ad,LVC}$

$$\mathbf{E}^{ad,LVC}(\mathbf{q}) = \mathbf{U}^T(\mathbf{q})\mathbf{V}^{dia}(\mathbf{q})\mathbf{U}(\mathbf{q}) \tag{30}$$

For small displacements, the adiabatic gradients at $\mathbf{q} = \mathbf{0}$ (FC point) can be obtained from the transformation above and the numerical differentiation of Eq.3. This results in gradients identical to the diabatic ones.

The transition dipole derivatives of the adiabatic states can be obtained by following the same approach. This is, for small displacement $\pm\Delta_\alpha$ along a mode q_α, the displaced adiabatic states are

$$|\mathbf{a}^{(r,LVC)}(\pm\Delta_\alpha)\rangle = |\mathbf{d}^{(r)}\rangle\,\mathbf{U}(\pm\Delta_\alpha) \tag{31}$$

The transition dipoles of the diabatic states are independent of the coordinates and are fixed to the value at the FC position. Therefore, using the rotation matrices $\mathbf{U}(\pm\Delta_\alpha)$, the adiabatic states transition dipole moments can be calculated at $\pm\Delta_\alpha$. Labeling as $\mathbf{Z}^{dia}$ the diabatic transition dipoles $\mathbf{z}_{1g}, \mathbf{z}_{2g}, \cdots, \mathbf{z}_{ng}$, where $\mathbf{z}$ can be either $\boldsymbol{\mu}_{\boldsymbol{jg}}^{\boldsymbol{FC}}$ or $\mathbf{m}_{ig}^{FC}$, the vector of the adiabatic transition dipoles is

$$\mathbf{Z}^{ad,LVC}(\pm\Delta_\alpha) = \mathbf{Z}^{dia}\mathbf{U}(\pm\Delta_\alpha) \tag{32}$$

and their derivatives are computed by numerical differentiation.

$$\left(\frac{\partial \boldsymbol{\mu}_{jg}^{ad,LVC}(\mathbf{q})}{\partial q_\alpha}\right)_{FC} \simeq \frac{\boldsymbol{\mu}_{jg}^{ad,LVC}(\Delta_\alpha) - \boldsymbol{\mu}_{jg}^{ad,LVC}(-\Delta_\alpha)}{2\Delta_\alpha} \tag{33}$$

$$\left(\frac{\partial \boldsymbol{m}_{jg}^{ad,LVC}(\mathbf{q})}{\partial q_\alpha}\right)_{FC} \simeq \frac{\boldsymbol{m}_{jg}^{ad,LVC}(\Delta_\alpha) - \boldsymbol{m}_{jg}^{ad,LVC}(-\Delta_\alpha)}{2\Delta_\alpha} \tag{34}$$

With these data we can run FC|VG and FCHT|VG adiabatic calculations, because the gradients are the same than for the diabatic states and the transition dipole derivatives can be written as linear functions of $\mathbf{q}$.

$$\boldsymbol{\mu}_{jg}^{ad,LVC}(\mathbf{q}) = \boldsymbol{\mu}_{jg}^{FC} + \sum_\alpha \left(\frac{\partial \boldsymbol{\mu}_{jg}^{ad,LVC}(\mathbf{q})}{\partial q_\alpha}\right)_{FC} q_\alpha \tag{35}$$

$$\boldsymbol{m}_{jg}^{ad,LVC}(\mathbf{q}) = \boldsymbol{m}_{jg}^{FC} + \sum_\alpha \left(\frac{\partial \boldsymbol{m}_{jg}^{ad,LVC}(\mathbf{q})}{\partial q_\alpha}\right)_{FC} q_\alpha \tag{36}$$

We highlight that the adiabatic spectra obtained by this protocol are fully

coherent with the LVC ones calculated from wavepacket propagations.

Following the same lines, from the LVC model we can also obtain the nonadiabatic couplings (NACs) between the adiabatic states at the reference geometry $\mathbf{q} = \mathbf{0}$. NAC between adiabatic states $|a_i^{LVC}\rangle$ and $|a_j^{LVC}\rangle$ are defined as

$$\langle a_i^{LVC}| \frac{\partial}{\partial q} |a_j^{LVC}\rangle \tag{37}$$

therefore, we need to be able to compute the derivative of the adiabatic state j with respect to any coordinate q_α and this is easily done by Eq.31

$$\frac{\partial}{\partial q} |a_j^{LVC}\rangle = |\mathbf{d}^{(r)}\rangle \frac{\mathbf{U}_{.j}(\Delta_\alpha) - \mathbf{U}_{.j}(-\Delta_\alpha)}{2\Delta_\alpha} \tag{38}$$

where $\mathbf{U}_{.j}$ specify the j column of the matrix $\mathbf{U}$. Realizing that $|a_j^{LVC}(\mathbf{0})\rangle = |d_j\rangle$ one automatically gets

$$\langle a_i^{LVC}| \frac{\partial}{\partial q} |a_j^{LVC}\rangle = \frac{U_{ij}(\Delta_\alpha) - U_{ij}(-\Delta_\alpha)}{2\Delta_\alpha} \tag{39}$$

S2 Additional Computational details

For the calculation of spin orbit coupling (SOC) elements between singlets and triplets at S_1 geometry, we used TD-DFT as implemented in ORCA 4.1.1 software package[S5] and switching off the Tamm-Dancoff approximation (TDA).[S6–S8] The convergence criteria for SCF was set to TIGHT, with a convergence threshold of 10^{-8} Hartree.

For the diabatization computation, we used a tight option for SCF convergence and a convergence threshold for TD-DFT energy equal to 10^{-6} eV, i.e., to get a robust results, as we did in our previous study on different conformers of Cytosine.[S9]

The derivatives of the transition dipole moments used to calculate the FCHT|VG spectra were obtained from the diabatization procedure, as described in Section S1.3. In Section S4.2 we compare these results with those obtained by numerical or analytical differentiation in different solvation regimenes.

The normal coordinates were organised as shown in the ML trees, which reports the ML expansion of the wavepacket and are shown in Figures S1-S3.

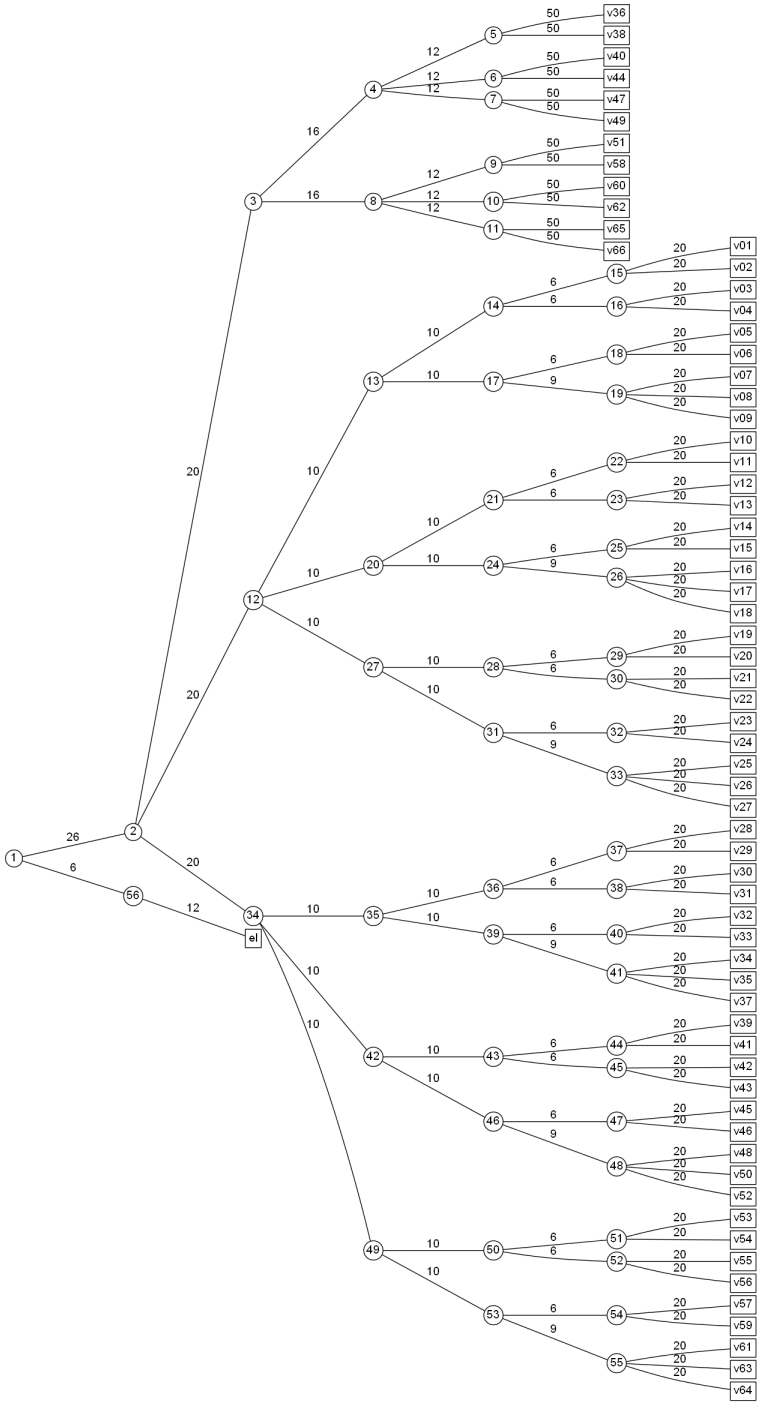

Figure S1: ML-MCTDH tree used for the calculations presented in the main document. The numbers above the lines represent the single particle functions (primitive functions for the right-most layer) used to combine each node. The numbers inside the circles are just labels and carry no physical information. 6 functions were used to describe the electronic states. 66 normal coordinates were included.

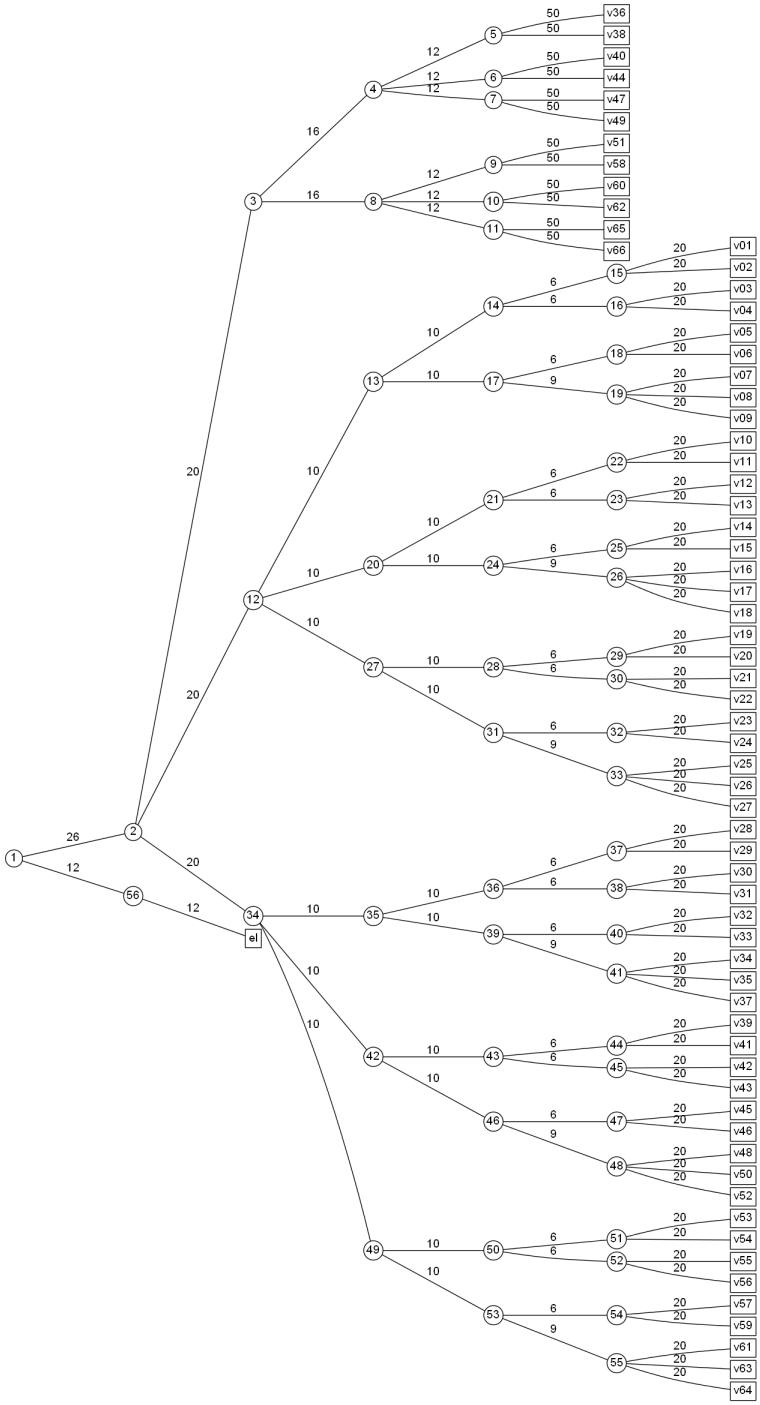

Figure S2: ML-MCTDH tree used for the tests in Figure S7. The numbers above the lines represent the single particle functions (primitive functions for the rightmost layer) used to combine each node. The numbers inside the circles are just labels and carry no physical information. 12 functions were used to describe the electronic states. 66 normal coordinates were included.

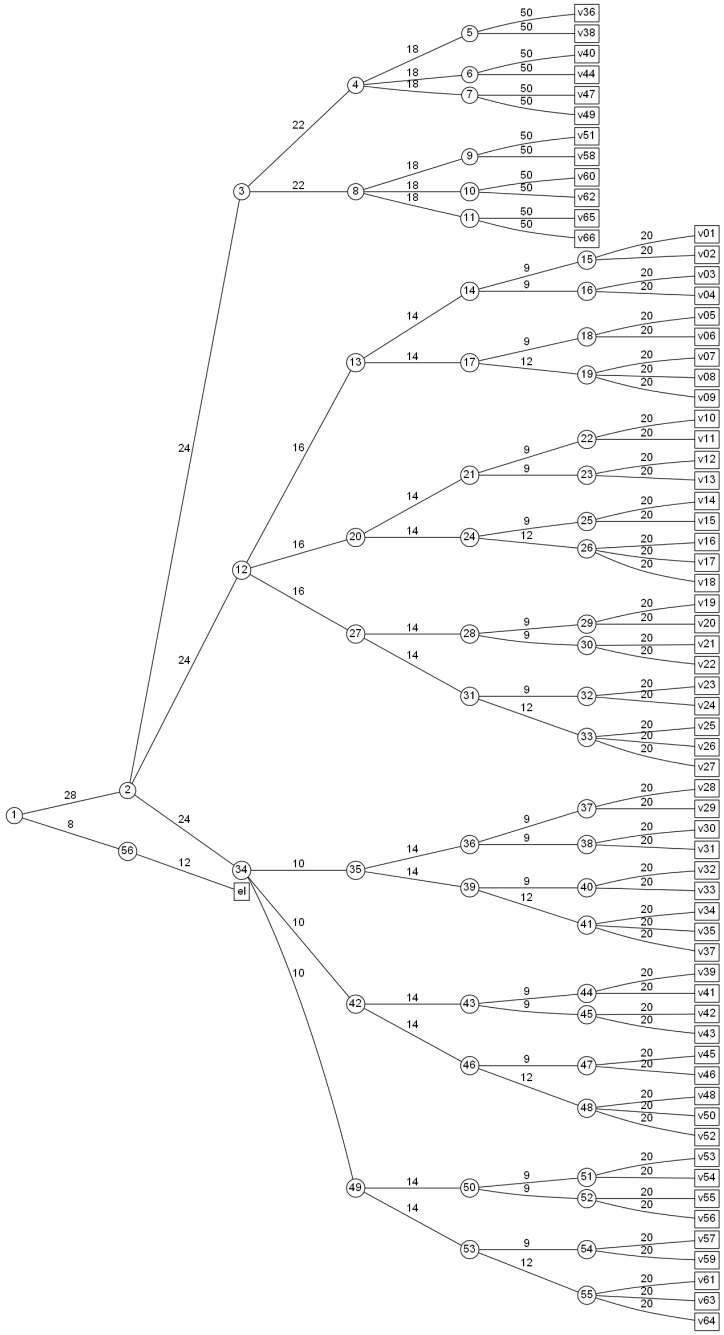

Figure S3: ML-MCTDH tree used for the tests in Figure S8. The numbers above the lines represent the single particle functions (primitive functions for the rightmost layer) used to combine each node. The numbers inside the circles are just labels and carry no physical information. 12 functions were used to describe the electronic states. 66 normal coordinates were included.

S3 Convergence tests

S3.1 DFT level of theory.

Table S1 reports the properties of the twelve lowest energy excited states for different basis sets and CAM-B3LYP functional. The results provided by TZVP, Def2TZVP and 6311+G(2d,dp) basis are all very similar, so we can reliably use the computationally convenient TZVP for the diabatization procedure.

Table S1: Vertical energies E_{gf} (eV), oscillator strengths δ_{OPA}, rotatory strengths (in the length gauge, R(length), 10^{-40} cgs) for the first twelve excited states, calculated with different basis set at CAM-B3LYP level in CH_2Cl_2.

State	TZVP			def2TZVP			6-311+G(2d,2p)		
	E_{gf}	δ_{OPA}	R	E_{gf}	δ_{OPA}	R	E_{gf}	δ_{OPA}	R
S_1	3.41	0.22	-487.95	3.38	0.22	-504.02	3.38	0.22	-507.44
S_2	3.72	0.00	4.51	3.69	0.00	5.84	3.69	0.00	6.05
S_3	4.14	0.21	188.45	4.11	0.22	202.30	4.10	0.22	201.22
S_4	4.53	0.73	791.52	4.51	0.71	791.00	4.49	0.72	803.17
S_5	4.55	0.21	-63.87	4.53	0.20	-61.19	4.52	0.20	-65.50
S_6	4.74	0.14	-566.30	4.70	0.14	-591.56	4.69	0.14	-602.90
S_7	4.87	0.03	-26.39	4.83	0.03	-22.56	4.81	0.04	-21.03
S_8	5.07	0.19	-53.63	5.05	0.21	-43.03	5.03	0.23	-34.30
S_9	5.08	0.16	-28.43	5.06	0.13	-31.97	5.05	0.14	-29.96
S_{10}	5.13	0.06	25.75	5.11	0.04	11.32	5.08	0.03	-5.58
S_{11}	5.34	0.03	-166.18	5.29	0.03	-159.09	5.27	0.03	-150.65
S_{12}	5.39	0.12	20.15	5.35	0.11	20.06	5.33	0.11	23.80

S3.2 ML-MCTDH convergence tests.

The number of modes to be included during the ML-MCTDH calculation are tested with Δ_α=0.1 in Figure S4 by setting a threshold on the value of the largest coupling/gradient. It shows that with 39 modes (threshold of 0.025 eV) the main spectral features are reproduced and increasing to 66 (threshold of 0.015 eV) only results in a small broadening and energies $>$ 4.5 eV, which improves the agreement with the experiments. Therefore, we consider that 66 modes are enough to properly reproduce the spectral shape for this system, and the effect of the remaining 54 coordinates not included, whose couplings are even smaller, are introduced phenomenologically by selecting an appropriate half-width at half maximum (HWHM) which matches with the experimental bands. Figure S5 shows that for the specific case of S_1, a HWHM of 0.06 eV reproduces the experimental width of the spectral bands.

The value of Δ_α is tested in Figure S6, and it can be seen that $\pm\Delta_\alpha$=0.02 and $\pm\Delta_\alpha$=0.10 results are identical. However, a smaller value of Δ_α provides more accurate values for the numerical derivative used to compute derivative of the transition dipoles, therefore, we selected $\pm\Delta_\alpha$=0.02 for the results presented in this work.

The number of SPFs for the electronic state degree of freedom are tested with 6 and 12 in Figure S7. We can see that the results only change slightly when the number of SPFs is increased from 6 to 12, so they can be considered to be converged. Therefore, to save computational time, we used 6 SPFs for the electronic states. Moreover, the test on the basis set for an initial excitation on the more strongly absorbing state S_4, in Figure S8, indicates that the smaller basis set reported in Figure S1 is good enough for our case. The ML trees for different test are shown in Figure S2 and S3.

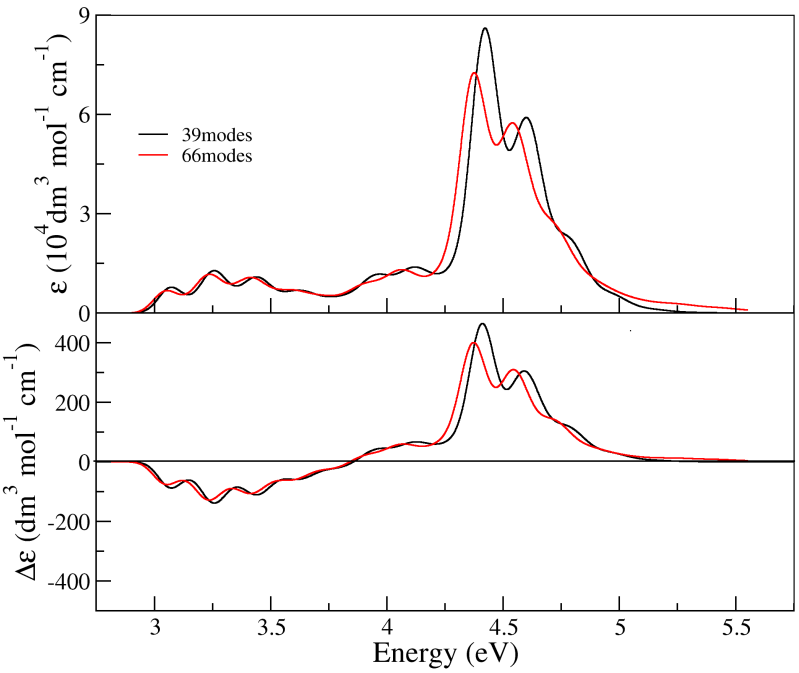

Figure S4: Aza[7]helicene nonadiabatic spectra computed with ML-MCTDH including 39 and 66 normal modes in CH_2Cl_2 (LR-PCM), using a dimensionless displacement of $\Delta_\alpha = 0.02$. The spectra were convoluted with a Gaussian of HWHM= 0.06 eV

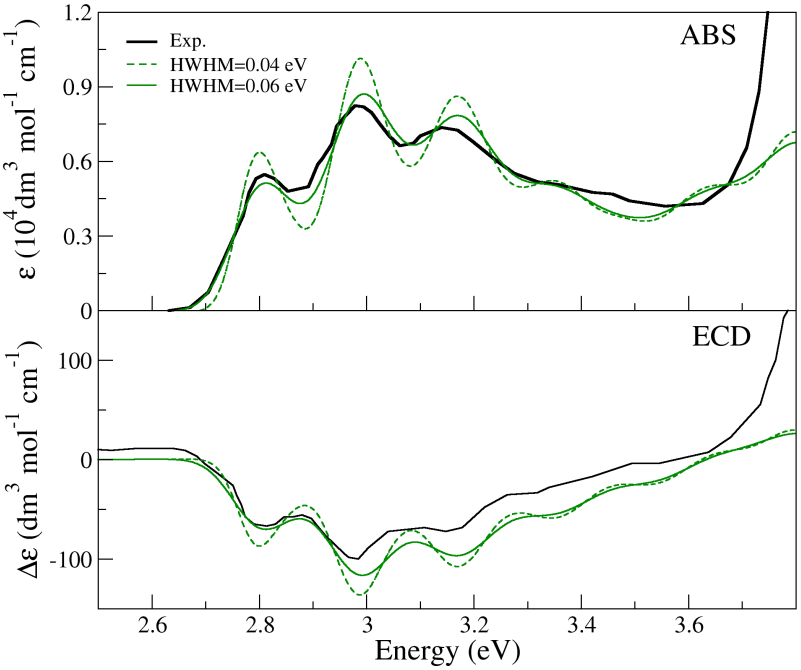

Figure S5: Aza[7]helicene spectra of ABS (top) and ECD (bottom) computed from in CH_2Cl_2 (SS-PCM) in low frequency region (states 1B-3A), including 66 modes and only auto terms during ML-MCTDH calculation. The theoretical spectra were convoluted with a Gaussian with a HWHM of 0.04 eV and 0.06 eV, respectively. To have a better comparison, the theoretical spectra has been red-shifted by 0.35.

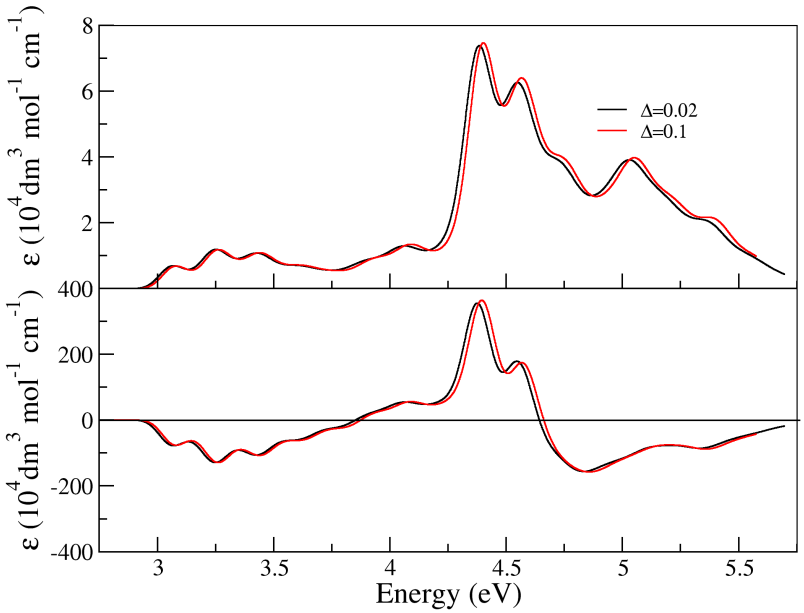

Figure S6: Aza[7]helicene LVC spectra in CH_2Cl_2 (LR-PCM), using a dimensionless displacement of 0.02(Δ=0.02) and 0.1 (Δ=0.1). 12 excited states and 66 normal modes are included during ML-MCTDH calculation. All spectra were convoluted with a Gaussian of HWHM= 0.06 eV.

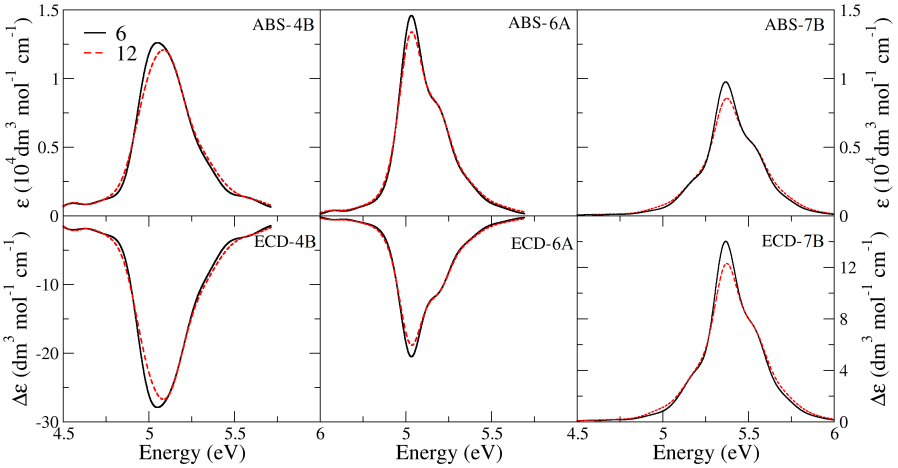

Figure S7: LVC spectra in CH_2Cl_2 (LR-PCM) of the states 4B, 6A, and 7B for different number of SPFs on the electronic states. We used 6 and 12 SPFs, respectively. 66 normal coordinates were included and all the stick transitions were convoluted with a HWHM = 0.06 eV.

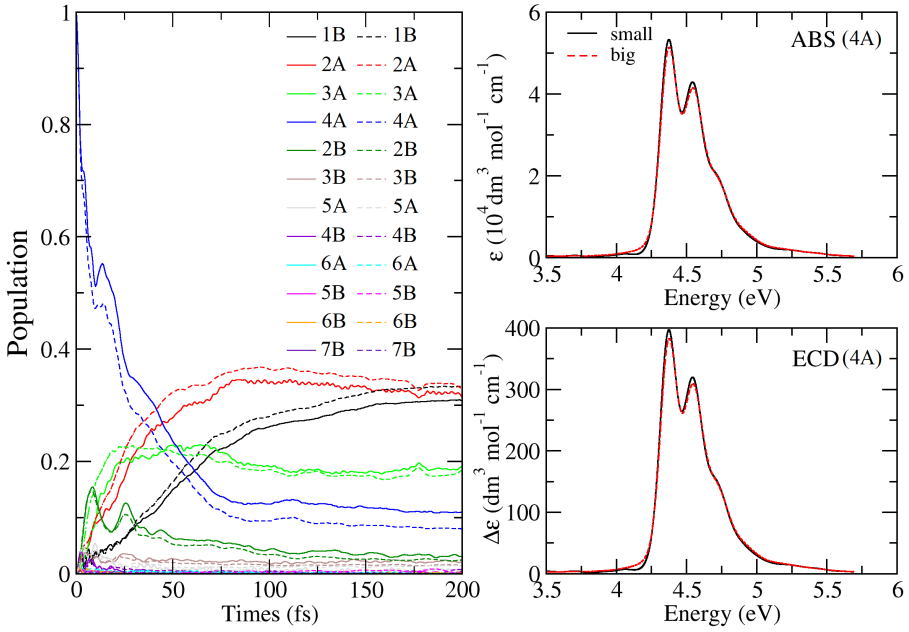

Figure S8: Convergence test of the ML-MCTDH tree. The left panel shows the population dynamics of the diabatic states for initial excitation on state 4A. The right panels show the ABS and ECD spectra for the same state. In all cases, the results shown by the solid lines were calculated with a smaller basis set shown in Figure S1, the dash ones were obtained with the bigger basis set shown in Figure S3.

S4 Additional results

S4.1 Pure electronic calculation

S4.1.1 Excited state properties and molecular orbitals (MOs) in gas phase and CH_2Cl_2.

Tables S2 and S3 report the calculated excitation energies, oscillator strengths and rotatory strengths for the first 12 excited states in gas phase and in CH_2Cl_2. The corresponding MOs are shown in Figure S9 for gas phase and in Figure S10 for PCM, and in both cases they are very similar.

Table S2: Excitation energies E_{gf} (eV), oscillator strengths δ_{OPA} and rotatory strengths (in the length gauge, R(length), 10^{-40} cgs) for the first 12 lowest excited states of aza[7]helicene in gas phase, calculated with CAM-B3LYP/TZVP.

State	E_{gf}	δ_{OPA}	R(length)	Transition	Coefficient
S_1	3.39	0.15	-414.70	H→ L	0.68
S_2	3.66	0.0011	20.9	H-1→L	0.62
S_3	4.06	0.089	89.95	H-2→L	0.62
S_4	4.50	0.14	-45.51	H-1→L+1	0.50
				H-3→L	-0.40
S_5	4.53	0.47	616.87	H-1→L+1	0.50
S_6	4.68	0.13	-530.93	H-3→ L	0.47
				H-1→L+1	0.41
S_7	4.83	0.058	11.19	H→L+2	0.59
S_8	5.00	0.050	-58.88	H-2→L+1	0.54
S_9	5.05	0.14	-23.39	H-1→L+3	0.26
S_{10}	5.16	0.13	39.92	H-4→L	0.53
S_{11}	5.26	0.015	-118.11	H-1→L+2	0.58
S_{12}	5.34	0.052	-26.71	H-2→L+2	0.35
				H→L+3	0.35

Table S3: Excitation energies E_{gf} (eV), oscillator strengths δ_{OPA} and rotatory strengths (in the length gauge, R(length), 10^{-40} cgs), for the first 12 lowest excited states of aza[7]helicene in CH_2Cl_2, calculated with CAM-B3LYP/TZVP. The adiabatic states are labeled as S_i (in parenthesis the usual nX label where X=A,B indicate their symmetry in Franck-Condon point and n orders the states with the same symmetry by increasing energy).

State	E_{gf}	δ_{OPA}	R(length)	Transition	Coefficient
S_1(1B)	3.41	0.22	-487.95	H→ L	0.68
S_2(2A)	3.72	0.003	4.51	H-1→L	0.62
S_3(3A)	4.14	0.21	188.45	H-2→L	0.64
S_4(4A)	4.53	0.73	791.52	H→L+1	0.61
S_5(2B)	4.55	0.21	-63.87	H-2→L+3	0.54
S_6(3B)	4.74	0.14	-566.30	H-1→ L+1	0.35
				H-3→L	0.50
S_7(5A)	4.87	0.03	-26.39	H→L+2	0.58
S_8(4B)	5.07	0.19	-53.63	H-2→L+1	0.53
S_9(6A)	5.08	0.16	-28.43	H-5→L	0.46
S_{10}(5B)	5.13	0.06	25.75	H-4→L	0.59
S_{11}(6B)	5.34	0.03	-166.18	H-1→L+2	0.58
S_{12}(7B)	5.39	0.11	20.15	H-4→L	-0.31
				H-2→L+1	0.31
				H→L+3	0.35

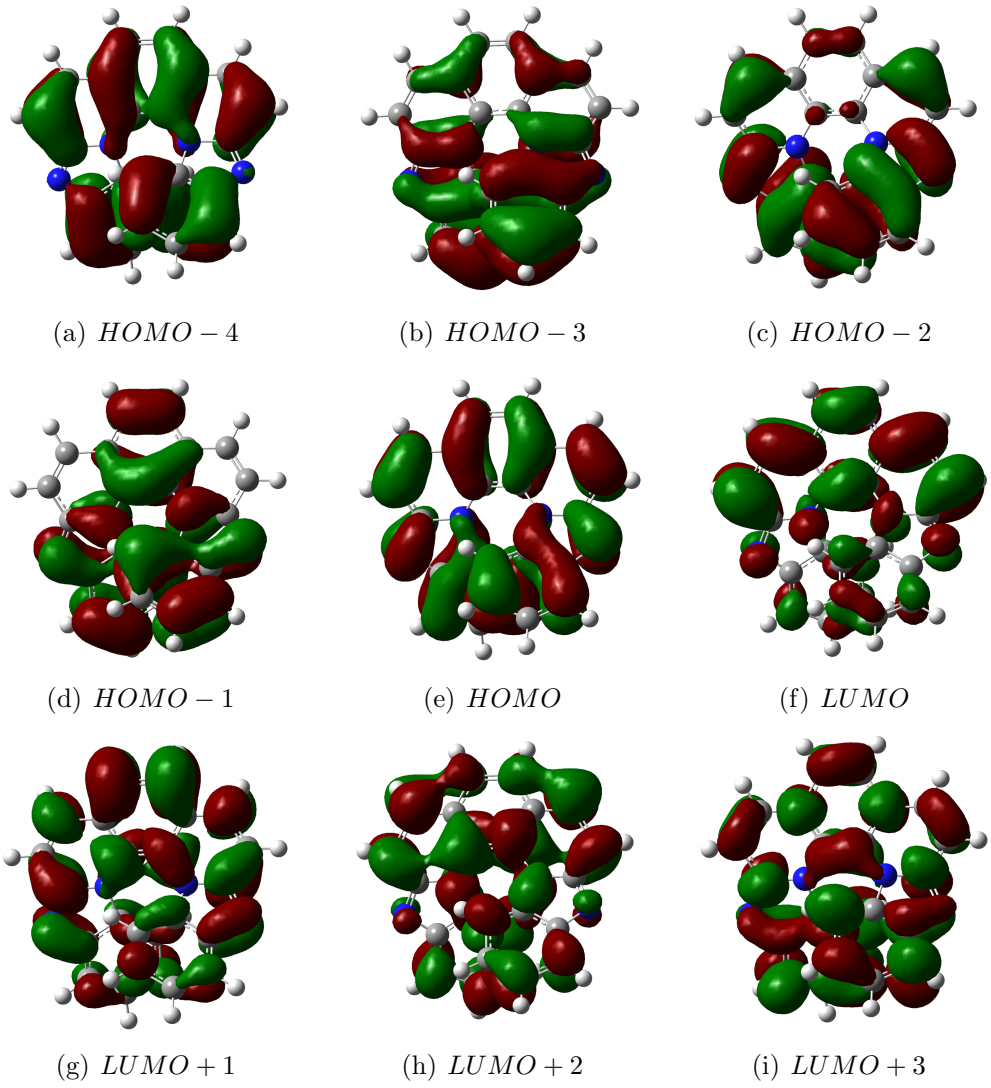

(a) $HOMO-4$ (b) $HOMO-3$ (c) $HOMO-2$

(d) $HOMO-1$ (e) $HOMO$ (f) $LUMO$

(g) $LUMO+1$ (h) $LUMO+2$ (i) $LUMO+3$

Figure S9: Molecular orbitals (MOs) for the first 12 lowest excited states of aza[7]helicene in gas phase, calculated with CAM-B3LYP/TZVP.

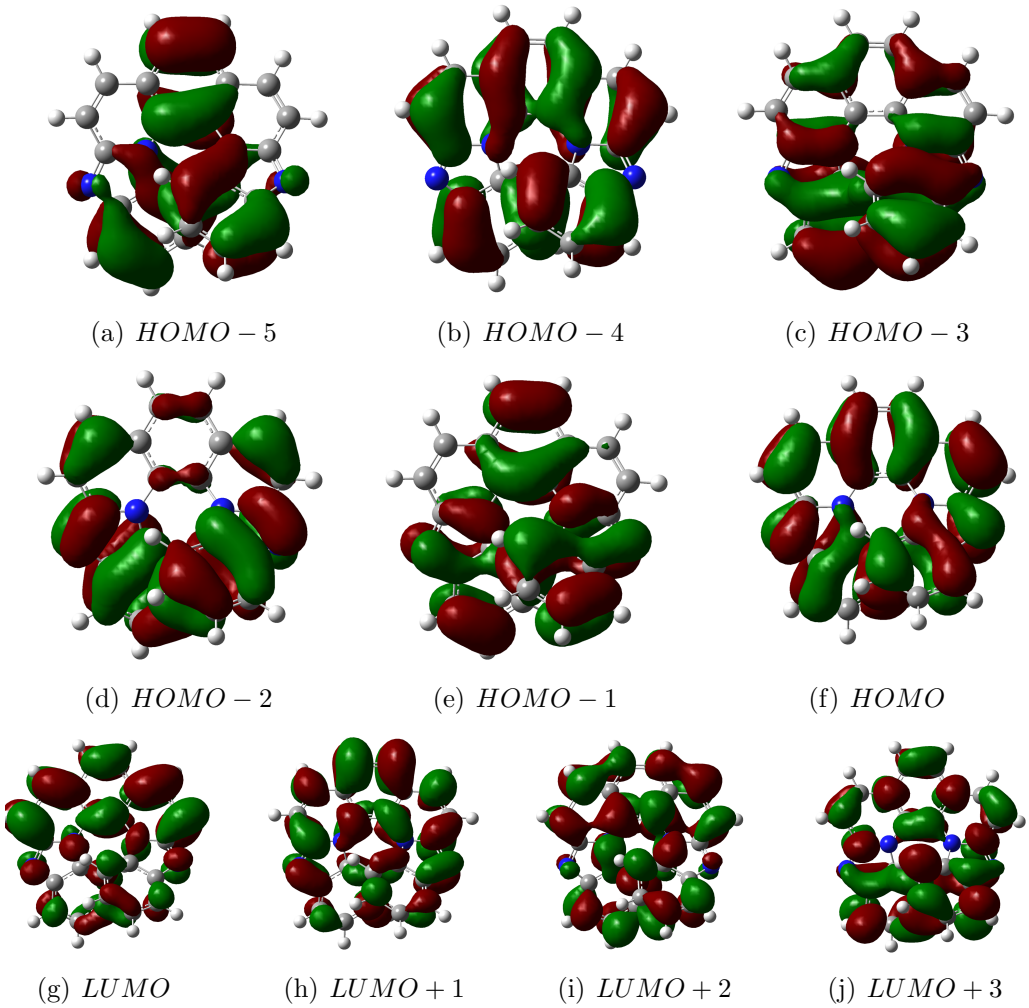

(a) $HOMO-5$ (b) $HOMO-4$ (c) $HOMO-3$

(d) $HOMO-2$ (e) $HOMO-1$ (f) $HOMO$

(g) $LUMO$ (h) $LUMO+1$ (i) $LUMO+2$ (j) $LUMO+3$

Figure S10: Molecular orbitals (MOs) for the first 12 lowest excited states of aza[7]helicene in CH_2Cl_2, calculated with CAM-B3LYP/TZVP.

S4.1.2 Pure electronic spectra

The purely electronic ABS and ECD spectra of aza[7]helicene computed at CAM-B3LYP/TZVP level of theory are plotted in Figure S11, summing over the first 12 electronic states in CH_2Cl_2 (LR-PCM) and in gas phase. Smooth spectral shapes were obtained attaching to each electronic stick line a phenomenological Gaussian with a half-width at half maximum (HWHM) of 0.25 eV. To have a more clear comparison with the experimental data, both the theoretical ABS and ECD spectra have been red-shifted by 0.4 eV. Our purely electronic spectra nicely reproduce the relative intensities of the three peaks observed experimentally in both ABS and ECD in CH_2Cl_2 at ∼3.0, ∼3.8 and ∼4.5eV. The smaller intensities predicted in gas phase improve the agreement with experiment for ABS, but worsen

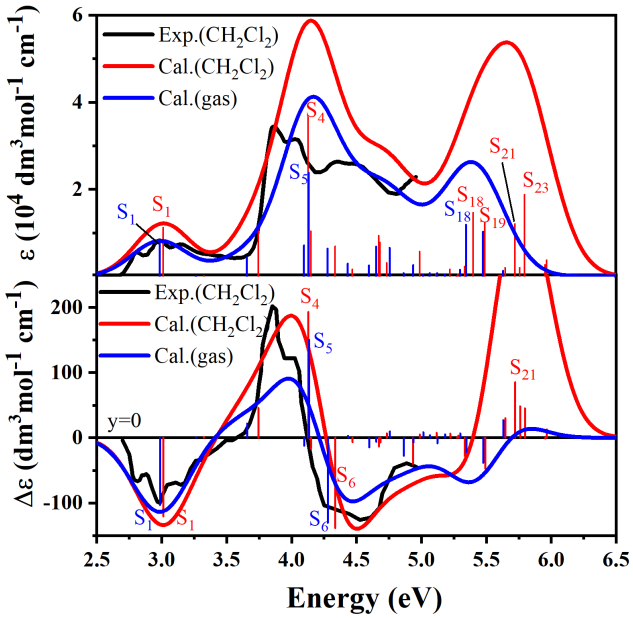

Figure S11: Pure electronic absorption and ECD spectra of (*M*)-aza[7]helicene, obtained at CAM-B3LYP/TZVP, summing over the first 25 excited states in CH_2Cl_2 calculated with LR-PCM model and in gas phase, convoluted with a Gaussian with a HWHM of 0.25 eV. To have a better comparison, the theoretical spectrum has been red-shifted by 0.4 eV. The states with larger contribution to the spectra are labelled.

it for the second ECD peak. Since the experimental spectra were obtained in CH_2Cl_2,[S10] in the following we will only focus on the simulation with PCM. Our results correctly capture the pattern of the signs of ECD, negative (∼3.0 eV), positive (∼3.8 eV) and negative (∼4.5 eV).

The first peaks in ABS and ECD at ∼3.0 eV mainly arises from the lowest excited state S_1, while S_3-S_5 seem to contribute to the second peak at ∼3.8 eV. S_{12} is the highest-energy bright state that contribute to the experimental spectra measured up to 250 nm (∼4.96 eV) in Ref.[S11] Data computed for these 12 states in PCM are reported in Table S3 and the corresponding molecular orbitals (MOs) are collected in Figure S10. Results in gas phase are very similar and given in Table S2 and Figure S9. Orbitals contributing to the excited states in this energy range only involve the π-system, whereas no contribution from lone pairs on the nitrogen atoms is observed. Inspection of the MOs indicates that some excited states have partial charge-transfer (CT) character. In fact, several orbitals are more localized either on the benzoimidazole-like (HOMO-2 and HOMO-1 orbitals) or on the phenanthrene-like (LUMO) aromatic systems within aza[7]helicene. Therefore, we studied solvent effects by also using the SS-PCM approach, finding that the results are in general very similar to LR-PCM, apart from an overall reduction of the ABS and ECD intensities for most of the states.

Table S3 shows that S_1 is the first bright state with an oscillator strength of 0.22 (δ_{OPA}) and rotatory strength of -487.95 (R, in 10^{-40} cgs) in CH_2Cl_2. It originates from the excitation of one electron from the highest occupied molecular orbital (HOMO, H) to the lowest unoccupied molecular orbital (LUMO, L) (see Table S3). The second bright state (S_3) is a H-2→L transition and has some partial CT character, with a transfer of electron density from the terminal benzimidazole rings to the central phenanthroline-like fragment (see Figure S10). S_4 is dominated

by the transition of H→L+1 and exhibits the strongest δ_{OPA} and positive R. The largest negative R is predicted for S_6, and it is the main responsible for the negative ECD peak at ∼4.5 eV. Similar discussion can be extended to the other excited states in both CH_2Cl_2 and gas phase with the help of Tables S2, S3 and Figures S9, S10. A more detailed analysis and assignment of the experimental bands is not possible from Figure S11 since they exhibit a pronounced vibronic structure (this was actually proved computationally for the lowest energy band in ref.[S10]) that is missing at purely-electronic level. As a last comment before moving to vibronic calculations, it is worthy to notice that Figure S11 suggests that S_4 and S_5 are blue-shifted ∼ 0.4 eV with respect to the second peak in both ABS and ECD. A better agreement would probably be possible adopting Coupled Cluster methods, since RI-CC2 has been shown to deliver good results on both the position and intensities of the excited states of a number of helicene derivatives.[S12,S13] Unfortunately, the application of the diabatization protocol for 12 states and 120 normal coordinates would be unfeasible at that level of theory. Luckily, Figure S11 shows that apart from the above discussed shift, CAM-B3LYP is able to provide a reasonable description of the spectral shape in all the energy region covered by experiments and therefore this is the method we chose for the vibronic analysis.

S4.2 Further analysis of FCHT spectra.

The ABS and ECD FCHT|VG spectra for each state are plotted in Figure S12. We can see that states S_4, S_5, S_8, and S_9 show an unphysical large increase of the intensity with respect to the FC|VG (see main document) which can be ascribed to an inappropriate treatment of the interstate couplings (see the discussion in Section S4.2.1). Tables S4 and S5 report the total FC and HT intensities of ABS (I_{tot}^{FC}, I_{tot}^{HT}) and ECD (R_{tot}^{FC}, R_{tot}^{HT}), which are calculated with the transition dipole

derivatives obtained by numerical differentiation in nonequilibrium regime and analytical differentiation in equilibrium regime (both LR-PCM) as implemented in Gaussian09 and Gaussian16, respectively. Interestingly, in nonequilibrium regime $|\mathrm{R}_{tot}^{HT}|$ is similar to $\mathrm{R}_{tot}^{|HT|}$. This happens because the transition dipole derivatives are dominated by large contributions arising from few normal modes (i.e. the modes that, as explained in the next section, are responsible fro the anomalous behavior of the spectra). On the contrary, in equilibrium regime $|\mathrm{R}_{tot}^{HT}|$ is in general much smaller than $\mathrm{R}_{tot}^{|HT|}$.

As expected, the numerical derivatives computed with nonequilibrium solvation are comparable to those obtained from the LVC model, and as shown in Figure S13 both approaches provide very similar spectra. Furthermore, by comparing non-equilibrium spectra with data obtained from Gaussian 09 and Gaussian 16, Figure S14 shows that the slight differences in the PCM implementation in the two versions of the code do not affect significantly the transition dipoles. On the contrary, the differences in the spectra computed with nonequilibrium and equilibrium regimes, are remarkable and very instructive. In fact, as shown in Table S5 and Figure S13, the HT intensity is very different for both cases. This is mainly due to states S_4 and S_5 as shown in Figure S14 and it will analyzed in detail in the next section.

Table S4: FC and HT intensities (I_{tot}^{FC}, I_{tot}^{HT}) in atomic units and rotatory strengths (R_{tot}^{FC}, R_{tot}^{HT}, $R_{tot}^{|HT|}$ (sum of HT absolute values)) in 10^{-40} cgs for the first 12 excited states, obtained at CAM-B3LYP/TZVP level for LR-PCM, calculated with numerical derivatives in nonequilibrium regime employing Gaussian09 .[S14]

State	I_{tot}^{FC}	I_{tot}^{HT}	R_{tot}^{FC}	R_{tot}^{HT}	$R_{tot}^{\|HT\|}$
S_1	2.68	0.40	-1.03	0.046	0.053
S_2	0.03	0.25	0.010	-0.006	0.067
S_3	2.08	0.29	0.40	0.006	0.070
S_4	6.58	24.82	1.68	-2.33	2.38
S_5	1.87	85.27	-0.14	20.83	22.06
S_6	1.19	1.25	-1.20	-0.032	0.20
S_7	0.27	0.44	-0.056	-0.034	0.16
S_8	1.50	13.72	-0.11	-0.56	0.64
S_9	1.25	19.77	-0.060	-0.89	0.95
S_{10}	0.49	2.88	0.054	-0.16	0.21
S_{11}	0.24	0.78	-0.35	0.022	0.11
S_{12}	0.87	0.63	0.043	-0.28	0.36
SUM	19.05	150.32	-0.759	16.61	27.26

Table S5: FC and HT intensities (I_{tot}^{FC}, I_{tot}^{HT}) in atomic units and rotatory strengths (R_{tot}^{FC}, R_{tot}^{HT}, $R_{tot}^{|HT|}$ (sum of HT absolute values)) in 10^{-40} cgs for the first 12 excited states, for LR-PCM, calculated with analytical derivatives in equilibrium regime using Gaussian16.[S15]

State	I_{tot}^{FC}	I_{tot}^{HT}	R_{tot}^{FC}	R_{tot}^{HT}	$R_{tot}^{\|HT\|}$
S_1	3.83	0.69	-1.16	0.072	0.083
S_2	0.050	0.46	0.017	0.022	0.097
S_3	5.38	0.54	0.91	0.028	0.084
S_4	8.24	2.84	1.80	-0.35	0.41
S_5	2.92	7.40	-0.10	0.67	2.09
S_6	1.60	1.64	-1.41	-0.059	0.16
S_7	0.36	0.65	-0.090	-0.031	0.13
S_8	3.35	1.05	-0.074	-0.16	0.23
S_9	1.37	1.29	-0.12	-0.18	0.28
S_{10}	0.053	4.24	-0.055	-0.21	0.30
S_{11}	0.37	1.22	-0.39	0.055	0.14
S_{12}	1.13	0.93	0.067	-0.42	0.51
SUM	28.66	22.96	-0.59	-0.57	4.51

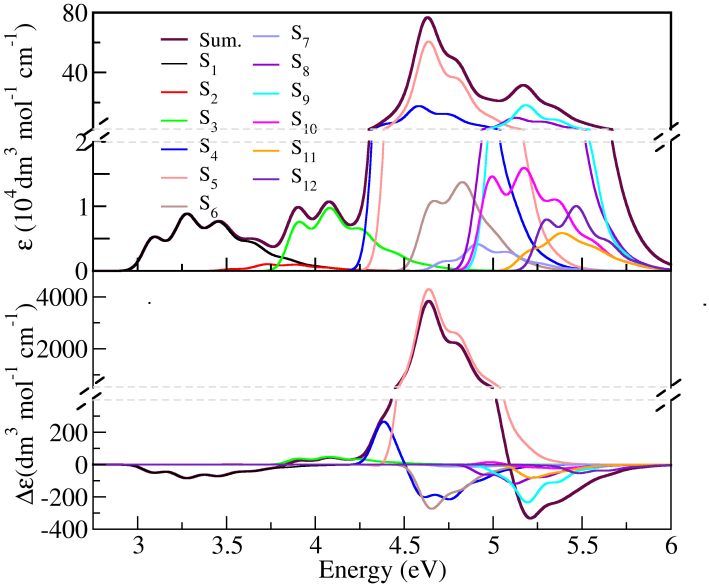

Figure S12: FCHT|VG ABS (top) and ECD (bottom) spectra for each state for (*M*)-aza[7]helicene, taking into account the first twelve excited states. All stick transitions were convoluted with a Gaussian of HWHM=0.06eV, red-shifted by 0.27 eV and scaled by a factor of 0.65.

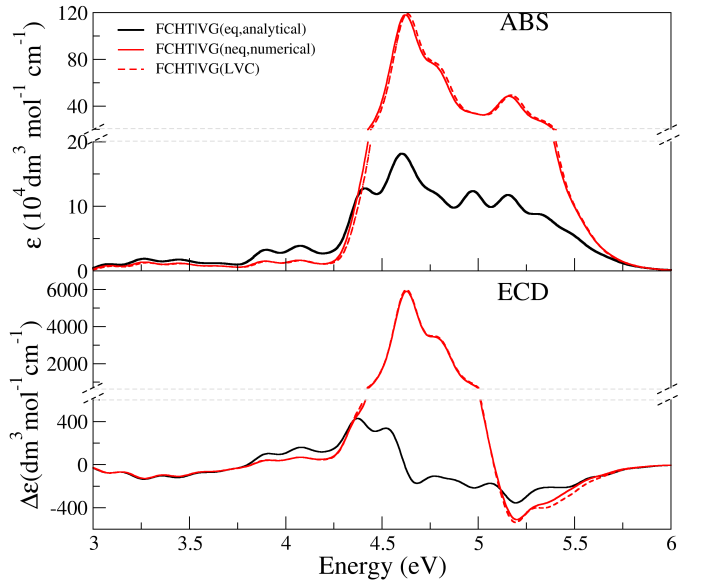

Figure S13: Comparison of ABS (top) and ECD (bottom) FCHT|VG spectra calculated with the transition dipole derivatives obtained from LVC model, or by analytical and numerical differentiation as implemented in Gaussian 16 and Gaussian09, respectively. The 12 lowest energy excited states were included and all stick transitions were convoluted with a Gaussian of HWHM = 0.06 eV.

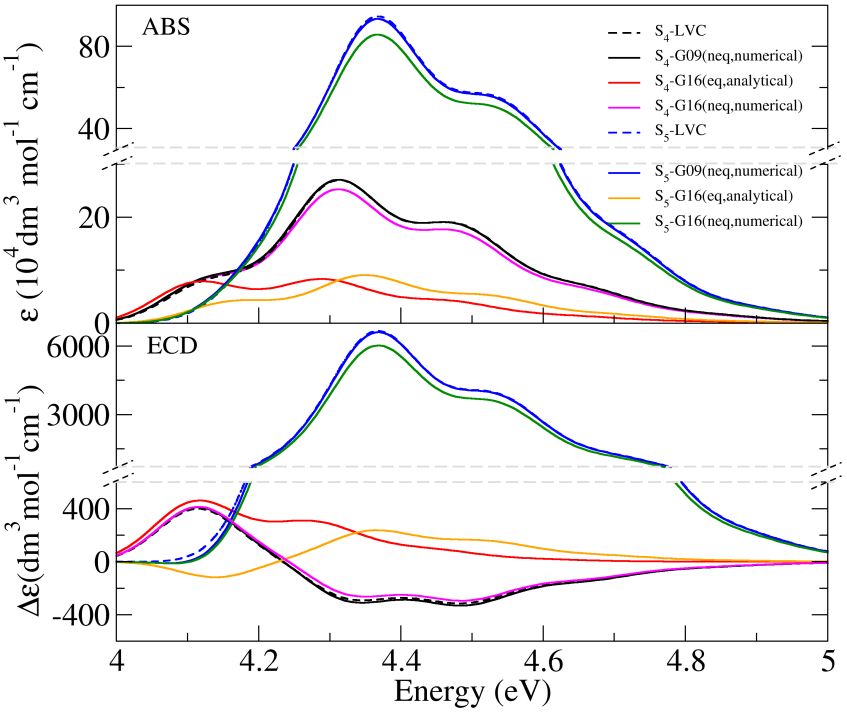

Figure S14: Comparison of ABS (top) and ECD (bottom) FCHT|VG spectra of states S_4 and S_5 calculated with the transition dipole derivatives obtained from LVC model using the procedure shown in section S1.3, or by analytical differentiation in equilibrium regime (eq) and numerical differentiation in nonequilibrium regime (neq) as implemented in Gaussian 16 (G16) and Gaussian09 (G09), respectively. The spectra have been red-shifted by 0.27 eV and all stick transitions were convoluted with a Gaussian of HWHM = 0.06 eV.

S4.2.1 An in-depth analysis of the origin of the overestimation of the FCHT intensities based on a small 2-states 1-mode LVC model for S_4 and S_5

Table S6 lists the modes carrying the largest coupling for diabatic states 4A and 2B. Such a coupling induces a dependence of the transition dipoles of the two corresponding adiabatic states S_4 and S_5 along these coordinates, and therefore, a HT contribution to the total intensities which is reported in Table S6 for computation with PCM in both nonequilibrium and equilibrium regimes. The first thing to notice is that (by definition) both are positive, i.e HT term increases the intensity of both states. Moreover, the HT contributions computed in the nonequilibrium regime are much larger. We know that actually at LVC level the total intensity is identical to the FC|VG one and the effect of the inter-state couplings is to redistribute the intensity.[S1]

Table S6: Normal modes α with the largest contribution to the ABS HT intensity, I^{HT}, (in atomic units) computed in PCM both in the nonequilibrium and in the equilibrium regime, and their contribution to the inter-state couplings ($\lambda_{45}(\alpha)$) between diabatic states 2B and 4A (in eV).

Mode (α)	$\lambda_{45}(\alpha)$	Non-equilibrium		Equilibrium	
		$I^{HT}_{S_4}(\alpha)$	$I^{HT}_{S_5}(\alpha)$	$I^{HT}_{S_4}(\alpha)$	$I^{HT}_{S_5}(\alpha)$
94	0.044	4.37	15.40	0.35	1.14
97	-0.041	3.84	12.51	0.45	1.02
105	-0.044	4.69	15.14	0.56	1.23

In order to illustrate the basic mechanism leading to the artificial increase of the intensity in FCHT description we focus on the adiabatic states S_4 and S_5 and we consider a minimal LVC model including only the two diabatic states 4A and 2B and their coupling along one of these relevant modes, Q_{94} (0.044 eV, Table S6). In practice, in this model we assume that displacing Q_{94}, the two adiabatic states S_4 and S_5 arise simply by the mixing of the two diabatic states they coincide to in the

FC position. In nonequilibrium regime at the FC point the two states are almost degenerate (ΔE_{54}=0.0205 eV), while their energy gap increases up to 0.087 eV in the equilibrium regime. At the FC position the $S_0 \rightarrow S_4$ transition is x-polarized while $S_0 \rightarrow S_5$ is polarized in the yz-polarized, with a dominant component along y. Figure S15 shows that due to the coupling the x and y components of the transition dipoles of the two states change with Q_{94}. At the FC point (Q_{94}=0), the Cartesian component of the state that is smaller (actually 0) shows a large first-derivative. However, for large displacements, such component deviates remarkably from its tangent at Q_{94}=0 and in particular is much smaller (absolute values). Since at HT level the transition dipoles are considered linear functions of the coordinates with the derivative computed at Q_{94}=0, this finding gives a first intuitive understanding of the origin of the overestimation of HT intensity. On the contrary, the Cartesian component of the stronger state shows a derivative equal to zero at Q_{94}=0 and then a small decrease.

The derivatives at Q_{94}=0 are much larger in the nonequilibrium regime than in the equilibrium regime, and the linear approximation of the transition dipoles (dashed lines) deviates much more from the exact result (solid lines). This is explained by the smaller energy gap in the former case. The same coupling, in fact, leads to a much larger mixing of the two diabatic states in the adiabatic states, when the energy gap is small (see Figure S16), and therefore, to much larger derivatives of the transition dipole of the adiabatic states. The FC and LVC total intensities for this 2-states model are simply given by the sum of the dipole strengths of the two states at the FC position,[S1] which are respectively 6.58 and 1.87 a.u. (Data from Table S4). It is worthy to be highlighted that actually results in Figure S15 confirm that the sum of the squared components of the transition dipoles of the two states do not change, i.e. confirm that the total intensity of

S_4 and S_5 does not change with Q_{94}. Notice that in the figure we actually report with a green line $\sqrt{\mu_{04}^2(\eta) + \mu_{05}^2(\eta)}$ where $\eta = x, y$. At variance the total intensity predicted with the linear approximation adopted in HT treatment does increase with Q_{94} (dashed green lines). The deviation from the exact total intensities is small and very large in the equilibrium and nonequilibrium cases, respectively.

Since, for each state n, the contribution of mode α to the HT intensity is $|\partial\mu_{0n}/\partial Q_\alpha|^2/2$,[S16] it is readily seen that even this small model predicts that the contribution to the S_4 and S_5 HT intensities of mode Q_{94} are respectively $2.94^2/2$=4.32 a.u. and $5.53^2/2$=15.29 a.u., and $0.87^2/2$=0.38 a.u. and $1.46^2/2$=1.07 a.u. in the equilibrium regime. These values are quite close to those reported in Table S6. The small differences are explained by the fact that in this small LVC model we neglected the z component of the transition dipoles and that, for the equilibrium case, in the small LVC model we assumed that the coupling does not change from the nonequilibrium to the equilibrium regime. It is noteworthy that such HT contribution for mode mode Q_{94} are even larger than the FC terms (for the nonequilibrium case). Moreover, since Table S6 shows that modes 97 and 105 exhibit similar couplings (λ_{45}), they will give rise also to similar HT contributions. On the balance, the three modes 94, 97 and 105 contribute by $\sim$ 45 a.u. to the total HT intensity of S_4 (85.27 a.u., see Table S4). This means that just the contribution of these three modes explain more that than 50 % of the huge increase of the intensity observed for S_4 in FCHT calculations.

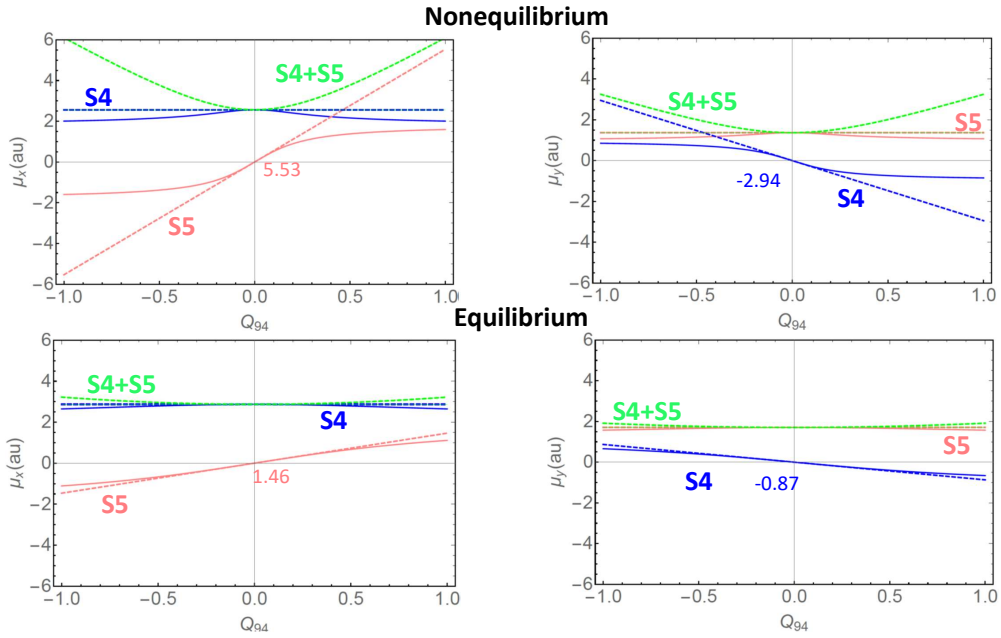

Figure S15: Solid lines report the dependence of the x (left) and y (right) components of the electric transition dipole of S_4 (blue) and S_5 (pink) adiabatic states obtained by diagonalization of a reduced dimensionality LVC model including the two corresponding diabatic states (3A and 2B) and the coupling along mode Q_{94}, with energy gaps and values of the transition dipoles at Q_{94}=0, obtained with LR-PCM calculations either in the nonequilibrium (top) or in the equilibrium (bottom) regime. Dashed lines report linear interpolations with derivatives taken at the FC point (Q_{94}=0). The values of the derivatives are given in the figure. Green solid line reports the square root of the sum of the squares of the Cartesian components of the transition dipoles for S_4 and S_5 $\sqrt{\mu_{04}^2(\eta)+\mu_{05}^2(\eta)}$ with $\eta = x, y$. Its square is the contribution of η to the total intensity. These lines are hardly visible because they overlap with the η component of the stronger state (S_4 for x, left panels, and S_5 for y, right panels). Since these lines are horizontal the total intensity does not change with Q_{94}. Dashed green lines report the same quantity, as computed by the transition dipole components obtained by the linear approximation. Notice that in this case the total intensity is erroneously predicted to increase with Q_{94}.

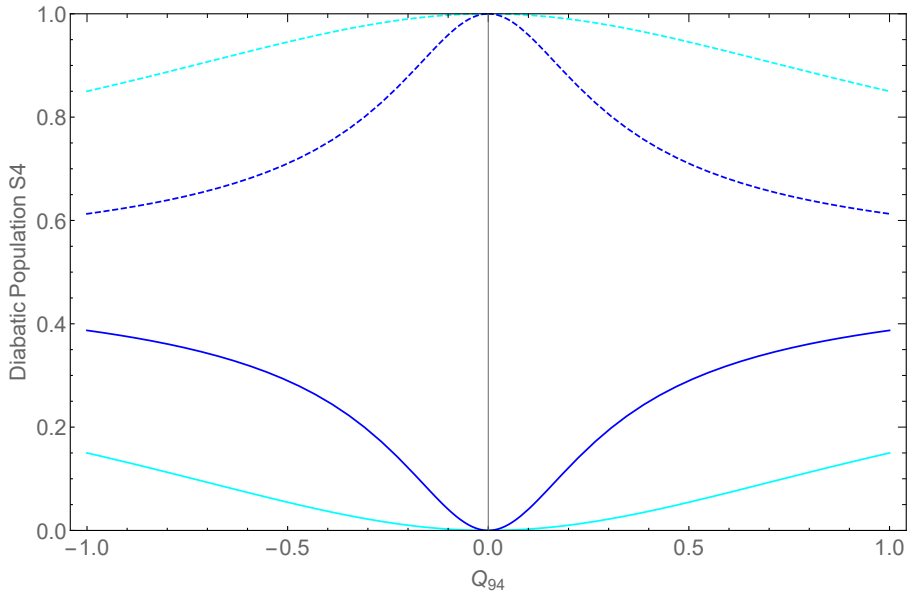

Figure S16: Contribution of the two diabatic states 3A (dashed line) and 2B (solid line) to the adiabatic state S_4 as a function of the displacement along Q_{94} for the 2-states-1-mode LVC model built considering a nonequilibrium (blue) or equilibrium (cyan) PCM energy gap. Notice that in dimensionless coordinates the standard deviation of the ground-state vibrational state along Q_{94} is 0.5.

S4.3 Estimated minima of the diabatic PESs, minimum energy crossing points and norms of the coupling vectors between the diabatic states

Table S7 reports the energy of each diabatic state (columns) at the minima of the LVC diabatic PESs (rows). The difference between the energy of each state on the S_0 minimum (i.e., the Franck-Condon point) and its own minimum is the reorganization energy λ. Table S7 shows that the largest reorganization energy (0.34 eV) exists in 1B, followed by 3A, 5B and 2A. All other states show $\lambda < 0.20$ eV. The minimum of 5B becomes more stable than 6A one because of the larger reorganization energy.

The off-diagonal elements of Table S8 provide the minimum energies crossing points (MECPs) between the diabatic states, whereas the diagonal terms report the minimum energy of the corresponding state (same data found in Table S7).

Table S9 reports the norm of the coupling vectors λ_{ij} of the LVC model, which provides a qualitative assessment of their relative importance, but the energy gap between the states in FC point must also to be taken into account (Table S7). When $i = j$, λ_{ii} reports diagonal (intra-state) coupling which corresponds to the energy gradients of each diabatic state in FC point. When i $\neq$ j, λ_{ij} reports off-diagonal (inter-state) coupling. We can see from Table S9 that the values of λ_{ii} are in general larger than those of λ_{ij}. This indicates that most of the states are weakly coupled, with some exceptions like those that are nearly degenerate, i.e., 4A/2B and 6A/4B. The largest gradients (λ_{ii}) are found for 1B, which can explain the larger reorganization energy observed. According to LVC, the largest interstate couplings λ_{ij} are expected between states 2B and 3B, and have similar magnitude to the energy gap between both states in FC point. This, as discussed in the

main document, has important effects on the spectroscopic signals and population dynamics. Inter-state couplings of similar magnitude are found for other pairs of states, for example 1B with 3A, 4A, 5A or 5B, but these states are far apart in energy and the effects of the coupling diminish.

Table S7: Energies (in eV) of aza[7]helicene diabatic states (columns) on the minimum energy structure of each state (rows) estimated by LVC model. The ground state structure (1A row) represents the energy on the Franck-Condon point. The reorganization energy λ (in eV) of each state is also shown.

STATE	1B	2A	3A	4A	2B	3B	5A	4B	6A	5B	6B	7B
1A	3.41	3.73	4.14	4.53	4.55	4.74	4.87	5.07	5.08	5.13	5.34	5.39
1B	3.07	3.75	3.94	4.57	4.78	4.95	4.83	5.21	5.17	5.04	5.59	5.46
2A	3.32	3.51	4.13	4.53	4.52	4.68	4.93	5.19	5.09	5.14	5.28	5.47
3A	3.16	3.78	3.85	4.55	4.70	4.89	4.85	5.10	5.15	5.07	5.58	5.39
4A	3.29	3.68	4.04	4.36	4.54	4.76	4.86	4.97	5.08	5.10	5.38	5.32
2B	3.44	3.61	4.14	4.48	4.41	4.66	4.93	5.06	5.08	5.22	5.25	5.41
3B	3.44	3.60	4.15	4.53	4.48	4.59	4.91	5.13	5.11	5.21	5.23	5.44
5A	3.21	3.74	4.00	4.51	4.64	4.80	4.70	5.10	5.10	5.09	5.35	5.39
4B	3.36	3.78	4.04	4.40	4.55	4.80	4.88	4.92	5.09	5.14	5.42	5.32
6A	3.26	3.61	4.02	4.45	4.51	4.72	4.83	5.03	4.98	4.99	5.30	5.35
5B	3.20	3.74	4.02	4.55	4.72	4.89	4.89	5.16	5.07	4.90	5.51	5.42
6B	3.51	3.64	4.28	4.59	4.51	4.66	4.90	5.19	5.13	5.27	5.15	5.52
7B	3.26	3.70	3.97	4.41	4.55	4.75	4.82	4.96	5.05	5.05	5.40	5.27
λ	0.34	0.22	0.29	0.17	0.14	0.15	0.17	0.15	0.10	0.23	0.19	0.12

Table S8: Energies (eV) of the minimum-energy crossing points (MECPs) between diabatic states of aza[7]helicene, estimated by LVC model. The vertical excitation energies (1A row, in blue) are added as reference, and MECPs with similar energies or below them are highlighted in bold. Notice that the table is symmetric. The values on the diagonal (in red) represent the energy of the minimum of the corresponding excited state.

STATE	1B	2A	3A	4A	2B	3B	5A	4B	6A	5B	6B	7B
1A	3.41	3.73	4.14	4.53	4.55	4.74	4.87	5.07	5.08	5.13	5.34	5.39
1B	3.07	**3.54**	5.27	5.71	5.04	5.48	8.85	7.03	8.92	10.43	6.68	10.76
2A	3.54	3.50	**3.86**	5.02	5.98	7.21	5.71	6.12	9.32	6.39	9.52	8.43
3A	5.27	3.86	3.85	**4.48**	**4.47**	**4.74**	5.50	5.97	6.35	6.12	5.60	8.87
4A	5.71	5.02	4.48	4.36	**4.42**	**4.59**	**4.76**	6.33	5.69	**5.07**	5.49	9.07
2B	5.04	5.98	4.47	**4.42**	4.41	**4.62**	**4.70**	**5.15**	5.50	**4.93**	6.17	6.24
3B	5.48	7.21	4.74	**4.59**	**4.62**	4.59	**4.71**	**4.94**	**5.11**	**4.90**	5.90	5.69
5A	8.85	5.71	5.50	4.76	4.70	**4.71**	4.70	**4.92**	**5.02**	**4.90**	**5.24**	5.71
4B	7.03	6.12	5.97	6.33	5.15	4.94	4.92	4.92	**4.98**	**4.97**	**5.15**	5.84
6A	8.92	9.32	6.35	5.69	5.50	5.11	5.02	**4.98**	4.98	**4.98**	**5.15**	**5.46**
5B	10.43	6.39	6.12	5.07	4.93	4.90	4.90	**4.97**	**4.98**	4.90	**5.16**	**5.37**
6B	6.68	9.52	5.60	5.49	6.17	5.90	5.24	**5.15**	**5.15**	**5.16**	5.15	**5.29**
7B	10.76	8.43	8.87	9.07	6.24	5.69	5.71	5.84	5.46	5.37	**5.29**	5.27

Table S9: Norm of the diabatic coupling vectors between the different diabatic states (eV) of aza[7]helicene, according to LVC model and using a dimensionless displacement of 0.02.

STATE	1B	2A	3A	4A	2B	3B	5A	4B	6A	5B	6B	7B
1B	0.34											
2A	0.10	0.25										
3A	0.18	0.10	0.30									
4A	0.16	0.10	0.07	0.22								
2B	0.07	0.13	0.07	0.10	0.19							
3B	0.10	0.12	0.12	0.08	0.19	0.18						
5A	0.12	0.08	0.09	0.11	0.04	0.06	0.23					
4B	0.09	0.08	0.10	0.14	0.11	0.08	0.06	0.21				
6A	0.09	0.11	0.10	0.07	0.09	0.09	0.05	0.05	0.17			
5B	0.13	0.08	0.10	0.07	0.07	0.08	0.07	0.06	0.08	0.23		
6B	0.04	0.11	0.04	0.09	0.08	0.12	0.10	0.09	0.06	0.05	0.22	
7B	0.09	0.06	0.09	0.08	0.07	0.08	0.08	0.13	0.09	0.09	0.06	0.18

S4.4 1D cut of the LVC potential energy surfaces

Figure S17 shows one dimensional (1D) cuts of the LVC diabatic potential energy surfaces (PES) along the collective coordinates connecting the minimum of the ground state (the FC point) to the minima of 12 excited states. The 1D energy profiles in Figure S17 can help to understand the results for the time evolution of the electronic populations reported in Figure 5 in the main text. They show, in fact, an intricate pattern of crossings of the PES. At the same time they show that PES corresponding at high-energy and low-energy states in the FC position do not easily cross, explaining why the former ones can decay toward the latter ones only passing thorough a number of intermediate states. Just to make and example, the 1D PESs along the coordinate from the FC point and the 3A minimum, show that 3A does not intersect with 1B directly and connects to 1B via 2A. This agrees with QD results showing a decay in two steps 3A $\rightarrow$2B$\rightarrow$1B. As a further example, along the coordinate from FC to 5A minimum, the PES of 5A first crosses with 3B, 2B and 4A. The PES of the latter states, moving in the direction of their minima then cross 3A and 2A. Such network of crossings is in line with the QD results showing that 5A decays first to 4A-3B and then to 2A and 3A.

Figure S18 reports similar 1D energy profiles but, in this case, we selected the coordinates connecting the FC point with the minimum-energy grossing points (MECPs) between states that are in consecutive order in the FC position (e.g. 2A/1B, 3A/2A, etc.). These plots show that many of these MECPs are easily accessible from the FC position and that in some cases multiple crossings occur. Of course, the fact that such MECPs are reachable does not automatically imply that the wavepacket actually cross them in a short time. As a matter of fact, only an *a posteriori* analysis of the wavepacket dynamics can unveil if they are met and on which timescale.

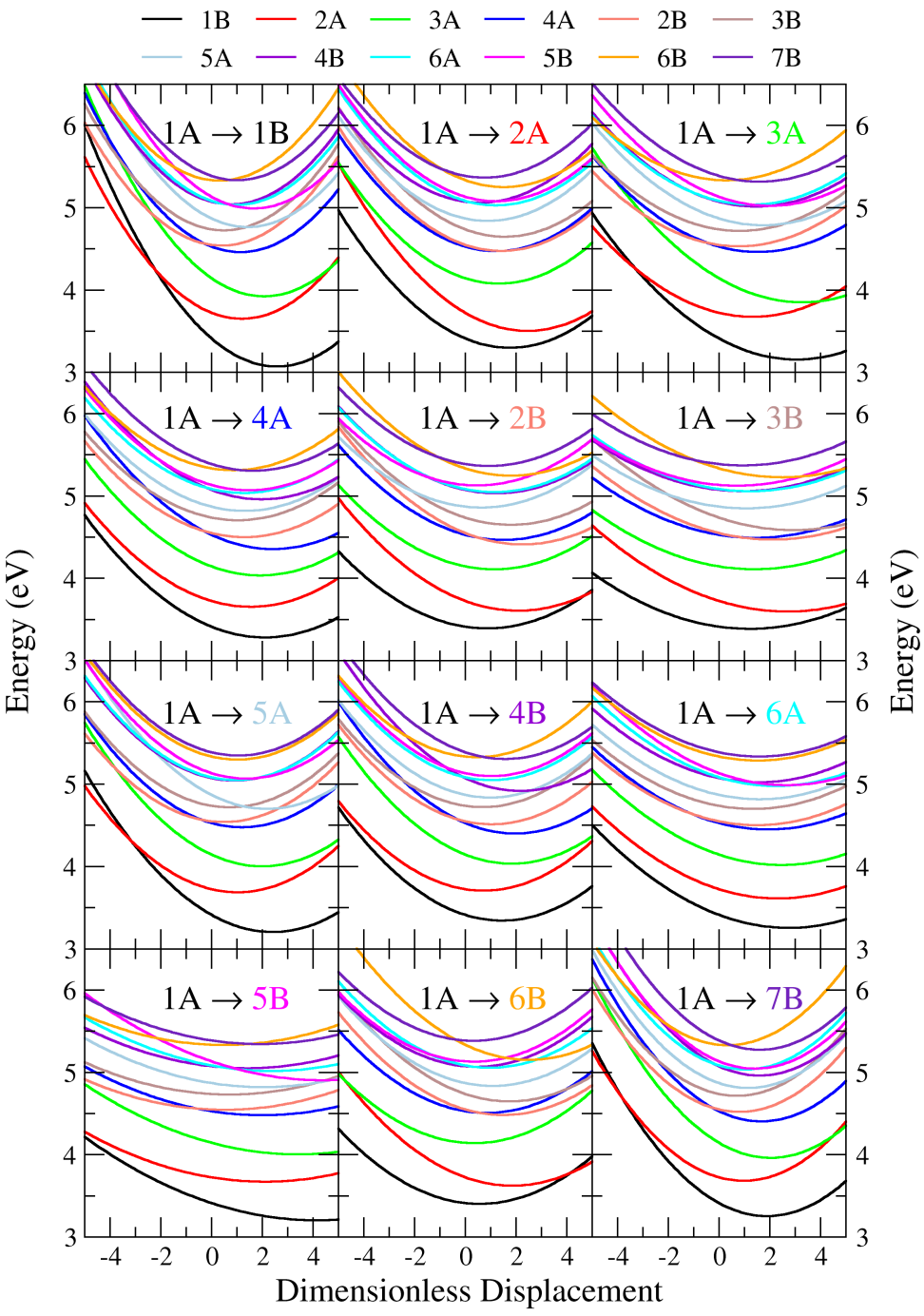

Figure S17: 1D energy profiles of the 12 LVC diabatic potential energy surfaces (PES) of (*M*)-aza[7]helicene along the collective coordinates (specified in each panel) connecting the FC point (i.e. the minimum of the ground state 1A) to the minima of each of the first 12 states.

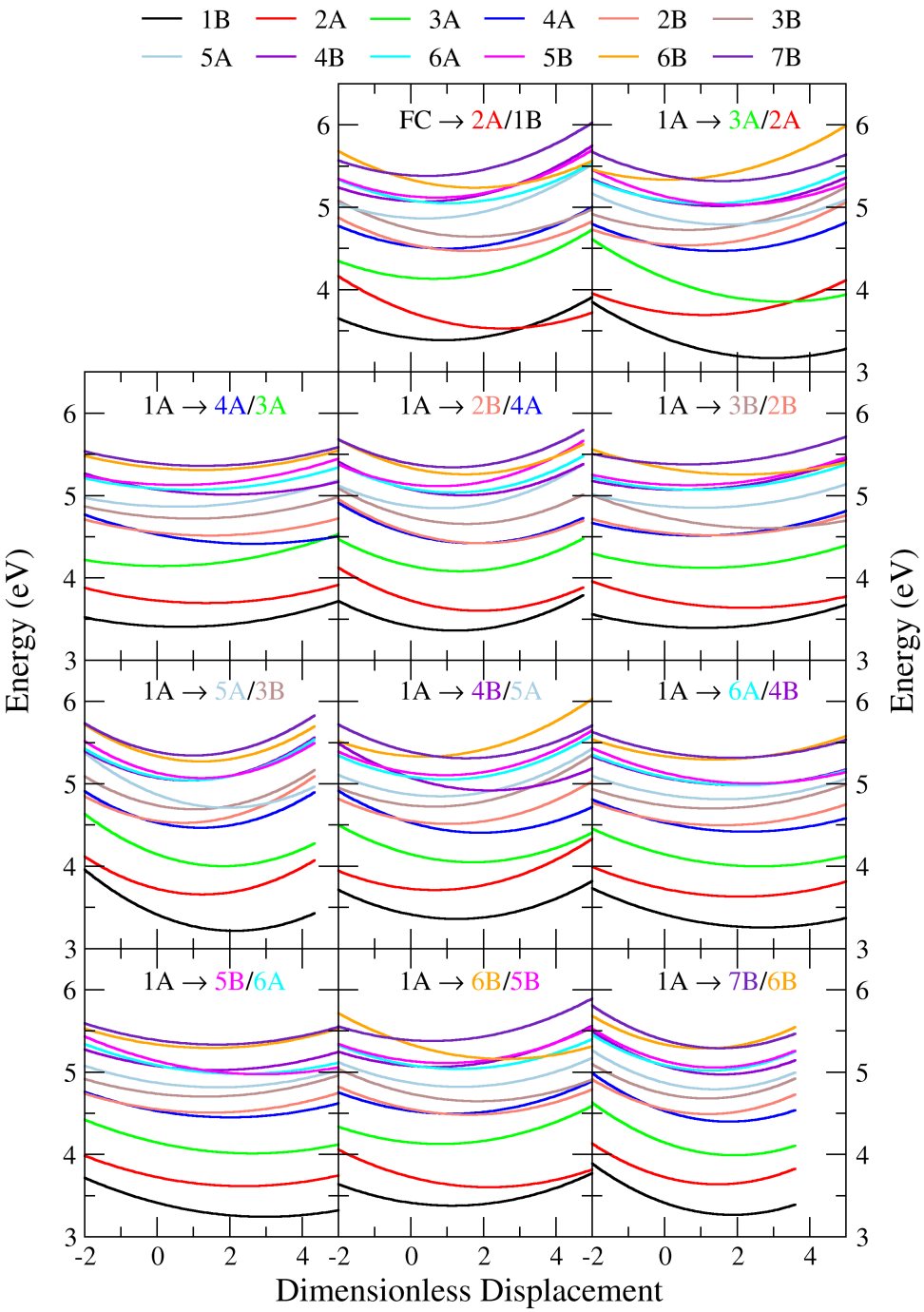

Figure S18: 1D energy profiles of 12 LVC diabatic potential energy surfaces (PES) of (*M*)-aza[7]helicene along a coordinate connecting the FC point (the minimum of the ground state 1A) to the minimum energy crossing points between states n and $n-1$, $n = 2, \ldots, 12$.

S4.5 LVC vibronic spectra calculated with the state-specific PCM approach.

The FC|VG and LVC spectra were computed also using the energies and transition dipole moments obtained with the State-Specific approach (SS-PCM). The excited state properties obtained at this level are shown in Table S10 and are characterized by an overall decrease of the oscillator strengths and a $\sim$ 0.1 eV blueshift of the energy for most of the states. Therefore, for LVC SS-PCM results, we corrected the energies and transition dipoles but utilised the same coupling parameters obtained for LR-PCM since the energy gap between most of the excited states is very similar for LR-PCM and SS-PCM (Table S10). The spectra are compared with those obtained with LR-PCM in Figures S19. The ABS and ECD intensities are very similar with respect to the LR-PCM spectra but to the decrease of the intensity. A more detailed view is given in Figures S20 -S21 for the low and high energy regions, respectively. Figure S20 shows that, beside the lower intensity, the spectral shape is identical to the corresponding LR-PCM. As discussed in the main document, LVC improves the agreement in the range 3.6-3.8 eV because the interstate coupling erases the vibronic bands in that region and not observed in the experiment. For the region above 3.6 eV, Figure S21 shows that SS-PCM and LR-PCM predict very similar spectral shapes, apart from an energy shift. Like for LR-PCM, LVC SS-PCM is superior to FC|VG, improving the agreement with the experimental spectral shape at 3.6-4.2 eV, especially for ECD. All the theoretical spectra underestimate the height of the band above 4.2 eV.

Table S10: Excitation energies E_{gf} (eV), oscillator strengths δ_{OPA}, Rotatory strength (R, in the length gauge, 10^{-40} cgs) of the first 12 excited states calculated with LR-PCM and SS-PCM, obtained with CAM-B3LYP/TZVP.

STATE	LR-PCM			SS-PCM			Reduced	Reduced
	E_{gf} (eV)	δ_{OPA}	R	E_{gf} (eV)	δ_{OPA}	R	δ_{OPA}	R
S_1	3.41	0.22	-488	3.51	0.16	-427	27.6%	12.6%
S_2	3.72	0.0027	5	3.76	0.0019	3	29.6%	33.2%
S_3	4.14	0.21	189	4.23	0.099	98	53.4%	47.9%
S_4	4.53	0.73	792	4.66	0.50	632	31.5%	20.2%
S_5	4.55	0.21	-64	4.62	0.14	-39	33.4%	39.3%
S_6	4.74	0.14	-566	4.81	0.13	-533	7.2 %	5.9%
S_7	4.87	0.032	-26	4.93	0.03	-15	9.3 %	43.3%
S_8	5.07	0.19	-54	5.13	0.047	-66	74.7 %	-23.6 %
S_9	5.08	0.16	-28	5.14	0.14	-14	10.4 %	52.2 %
S_{10}	5.13	0.062	26	5.19	0.090	44	-44.1%	-72.1 %
S_{11}	5.34	0.031	-166	5.38	0.025	-161	17.9 %	3.3 %
S_{12}	5.39	0.12	20	5.45	0.080	6	30.0 %	72.5 %

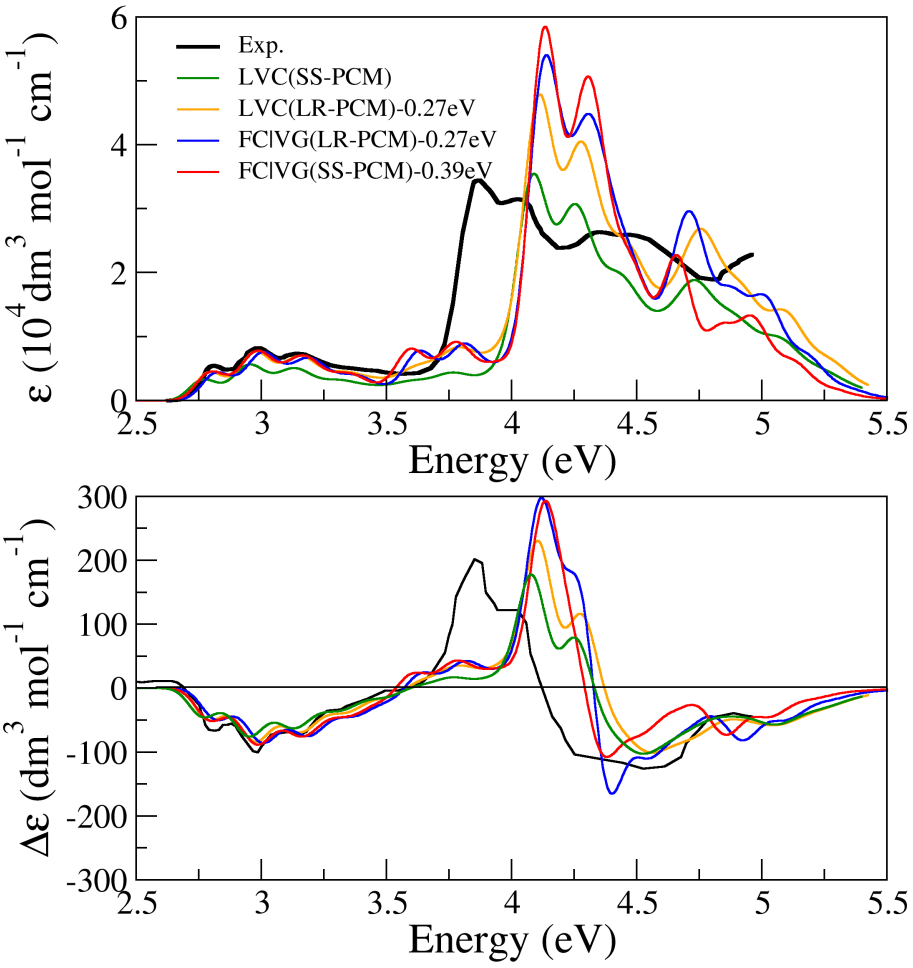

Figure S19: (*M*)-aza[7]helicene LVC ABS (top) and ECD (bottom) spectra computed in CH_2Cl_2 solution LR-PCM and SS-PCM (66 modes, only auto terms) convoluted with a Gaussian of HWHM=0.06eV. Note that all the theoretical spectra have been red-shifted by 0.27(0.39) eV for LR-PCM (SS-PCM) and scaled by a factor of 0.65.

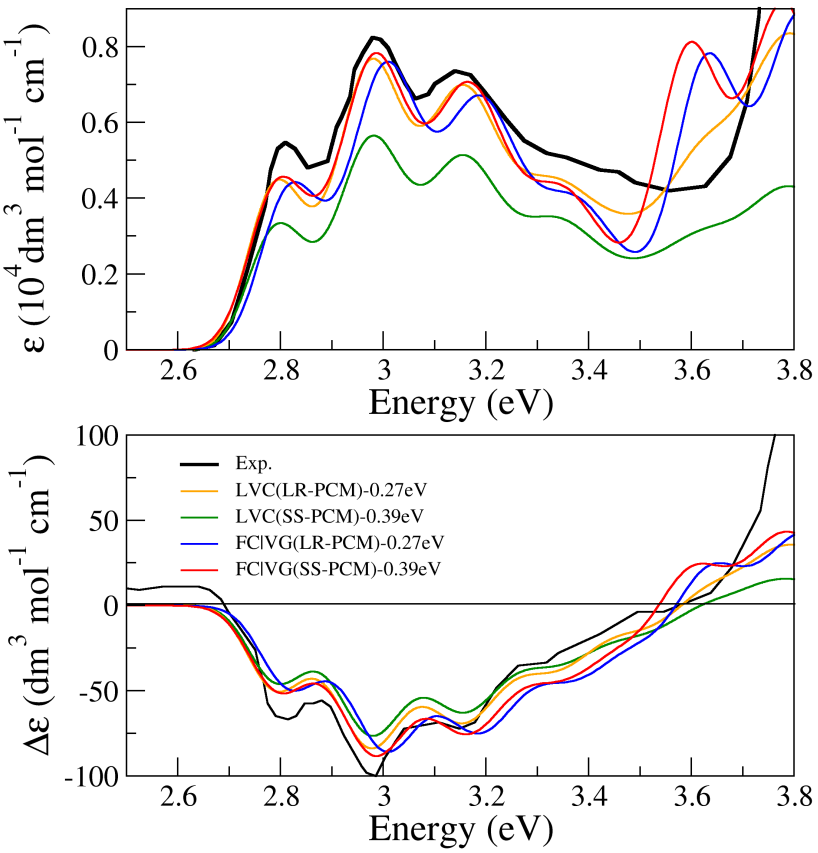

Figure S20: (*M*)-aza[7]helicene ABS (top) and ECD (bottom) spectra of the low frequency region computed in CH_2Cl_2 solution with LR-PCM and SS-PCM (66 modes, auto terms only). All the spectra are convoluted with a Gaussian of HWHM=0.06eV. Note that all the theoretical spectra have been red-shifted by 0.27(0.39) eV for LR-PCM (SS-PCM) and scaled by a factor of 0.65.

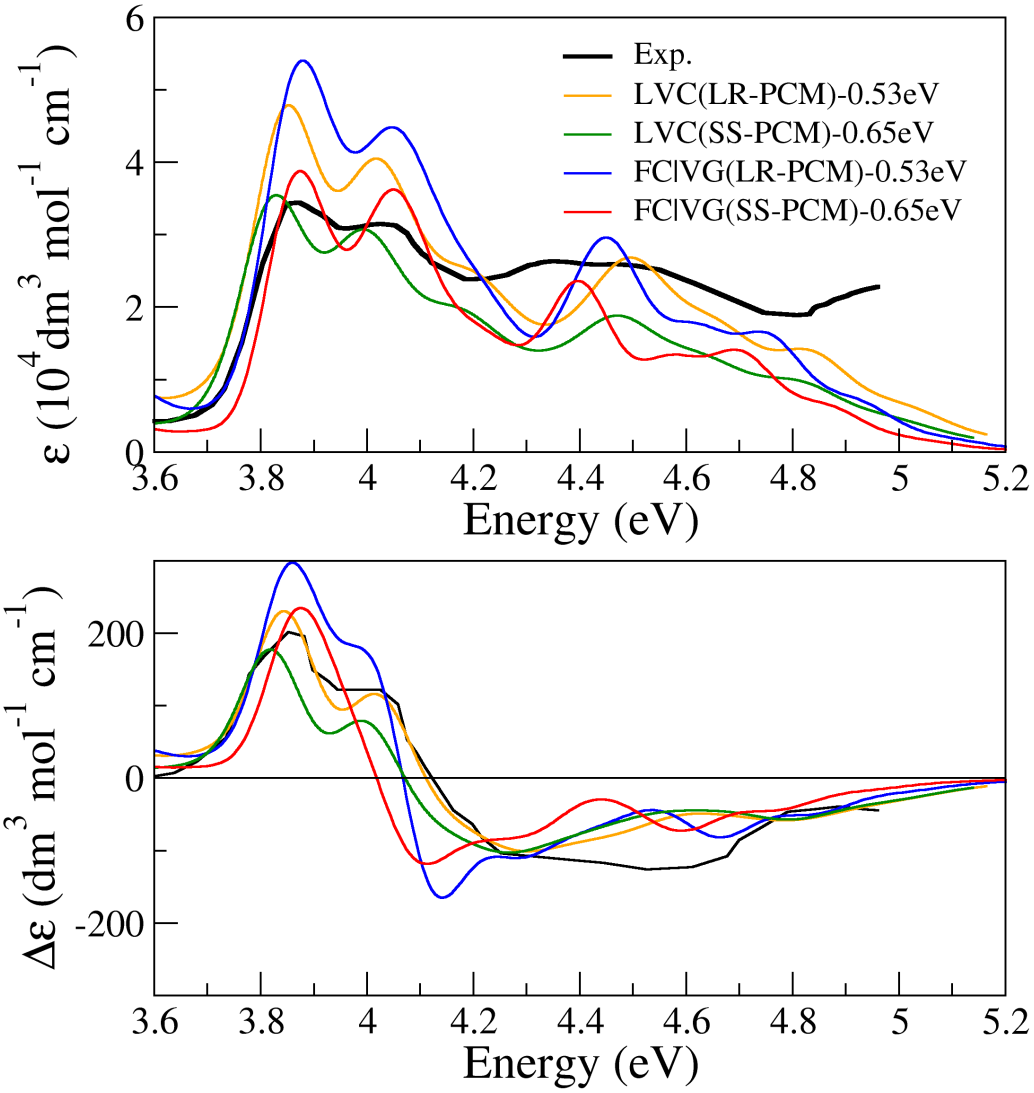

Figure S21: (*M*)-aza[7]helicene ABS (top) and ECD (bottom) spectra of the high frequency region computed in CH_2Cl_2 solution with LR-PCM and SS-PCM (66 modes, auto terms only). All the spectra are convoluted with a Gaussian of HWHM=0.06eV. Note that all the theoretical spectra have been red-shifted by 0.53 eV (LR-PCM) and 0.65 eV (SS-PCM), and scaled by a factor of 0.65.

S4.6 Relevant modes for vibronic progressions and couplings

The vibronic stick bands of FC|VG spectra for S_1 and S_4 are shown in Figure S22. Table S11 reports the high-frequency normal modes mainly responsible for the progression observed in the spectra of S_1 and S_4.

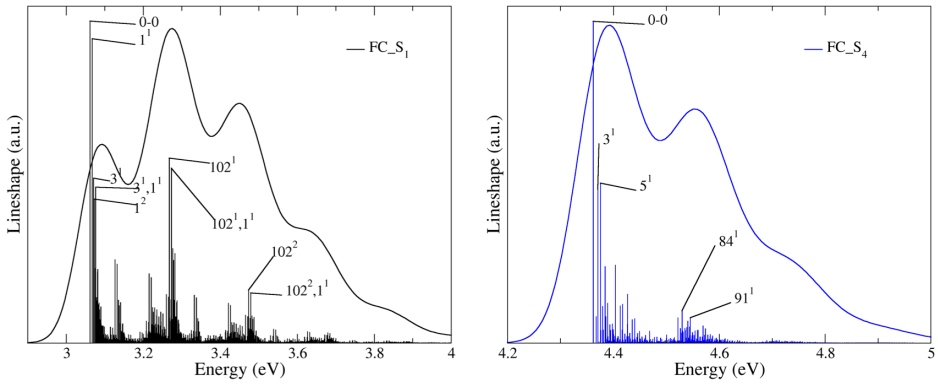

Figure S22: FC|VG spectra for S_1 and S_4 computed with a time-independent method[S16] reported both as stick vibronic bands and their convolution with a Gaussian with the same HWHM reproted in the main text. CAM-B3LYP/TZVP in CH_2Cl_2 solution (LR-PCM). The sticks correspondign to the main vibronic progressions are labelled as "n^x", where x indicates the quanta deposited on the excited-state normal mode n.

Table S11: Normal modes α with the largest contribution to the ABS FC intensity (δ, the displacement in dimensionless units).

State (i)	Mode (α)	δ
S_1	102	-11.93
S_4	84	-5.59
S_4	91	-4.72

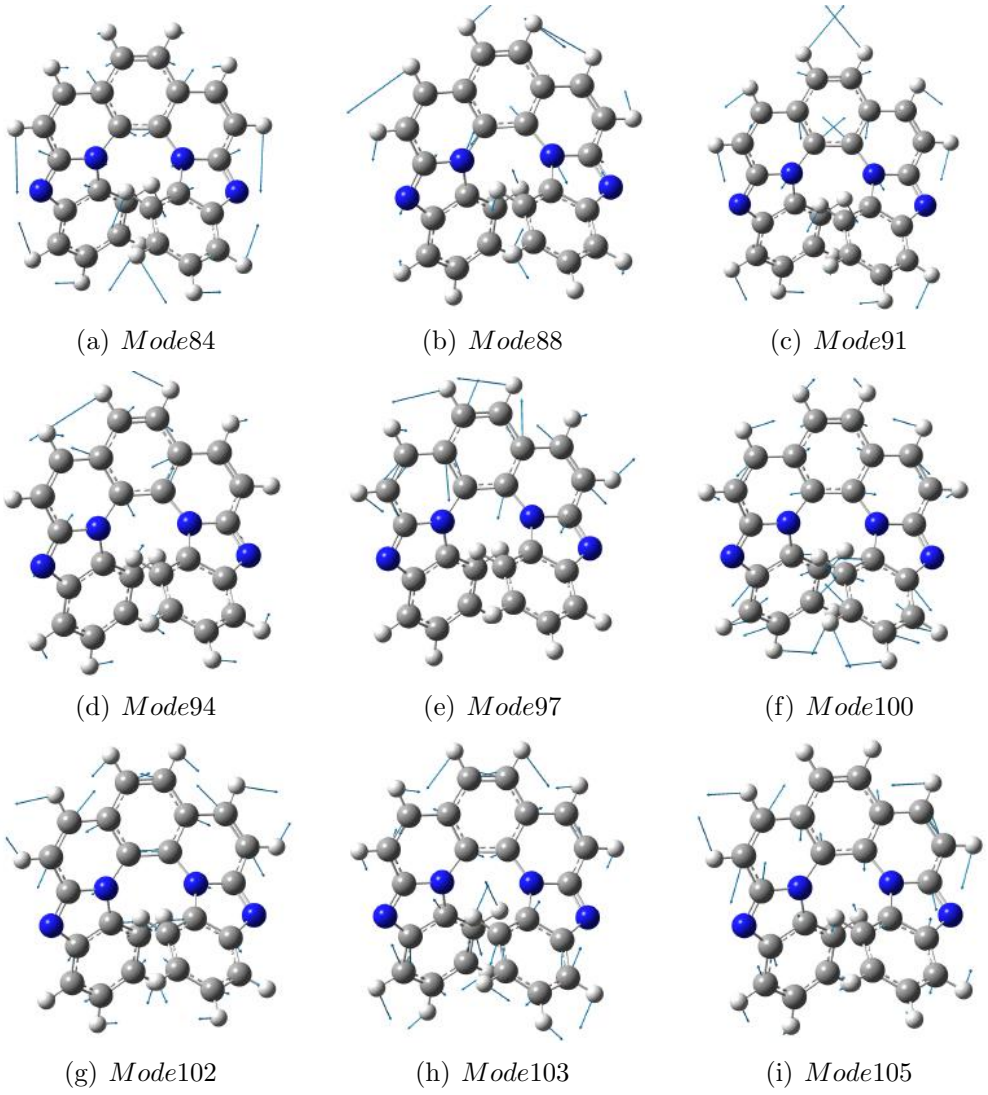

(a) $Mode84$ (b) $Mode88$ (c) $Mode91$

(d) $Mode94$ (e) $Mode97$ (f) $Mode100$

(g) $Mode102$ (h) $Mode103$ (i) $Mode105$

Figure S23: Displacement vectors for the ground state normal modes more relevant for vibronic progressions and inter-state couplings. CAM-B3LYP/TZVP in CH_2Cl_2 solution (LR-PCM).

S4.7 Time evolution of the electronic populations from quantum dynamics

Populations dynamics of the diabatic states are reported up to 1500fs in Figure S24. It confirms the fact discussed in the main document that all the states decay either directly to 1B, or first to 2A, 3A or even to 4A then finally to 1B. For instance, we can see that starting from 3B, the population of 1B surpasses 2A in about 1500 fs. A different sets of dynamical simulations, starting from photo-exciting the vibrational ground states of the different diabatic states are shown for comparison in Figure S25.

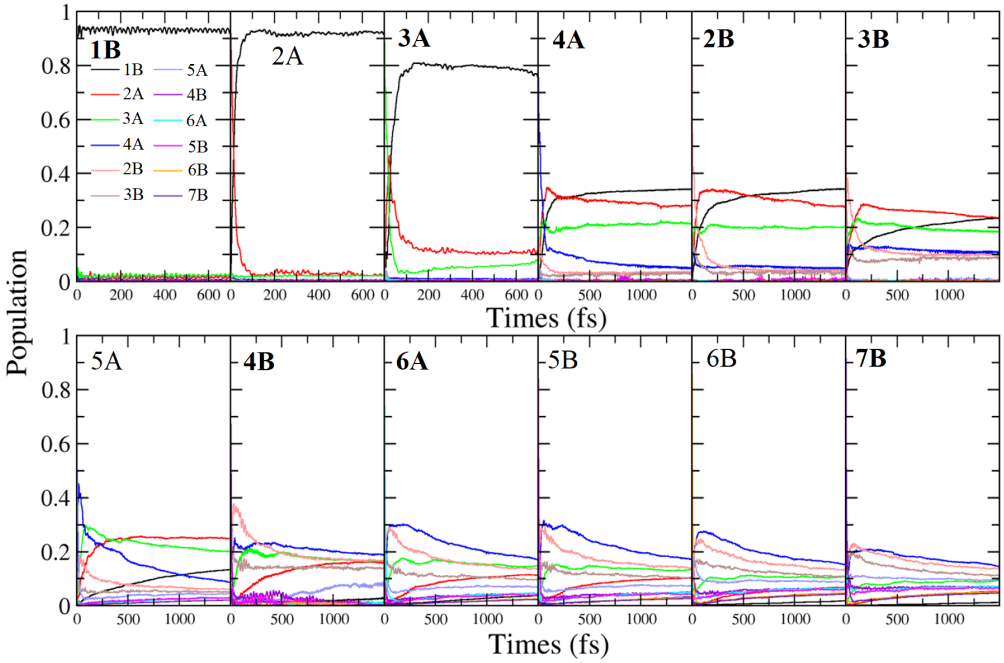

Figure S24: Population dynamics of the diabatic states for (*M*)-aza[7]helicene in CH_2Cl_2. The initial state is labeled in each panel and bright states are indicated with bold labels.

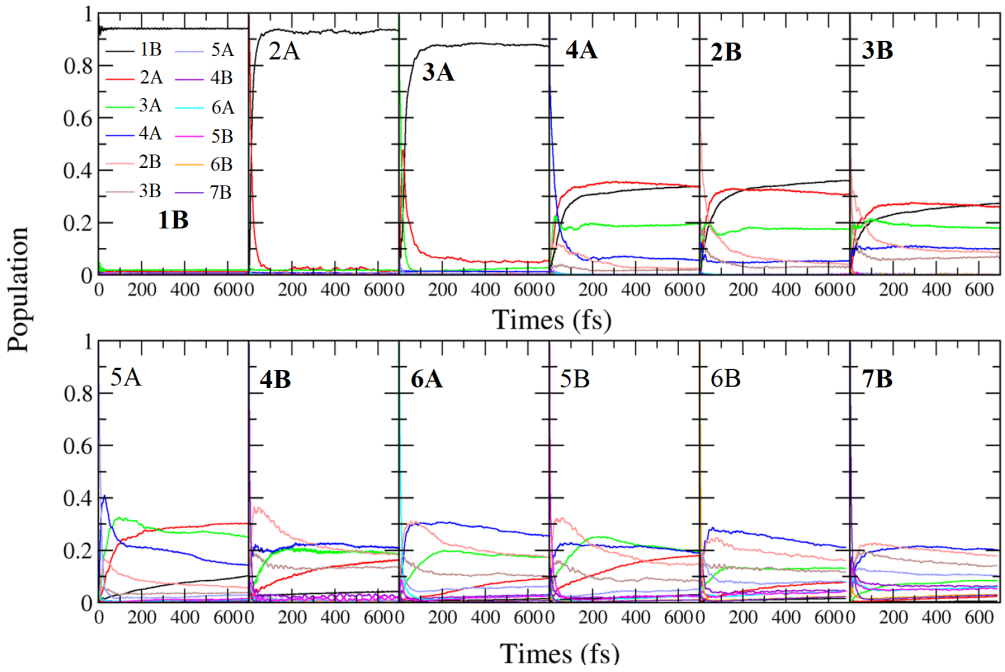

Figure S25: Population dynamics of the diabatic states for (*M*)-aza[7]helicene in CH_2Cl_2 starting from the vibrational ground state of each electronic state. The initial state is labeled in each panel and bright states are indicated with bold labels.

S4.8 Internal conversions between excited states based on a kinetic model

Figure S26 compares the time evolution of the electronic populations for an initial excitation on the lowest vibrational state of either 2A or 3A, performed with ML-MCTDH wavepacket propagations under the effect of the LVC Hamiltonian with the results of the kinetic model built up on the grounds of kinetic rates obtained from Fermi Golden rule (FGR) at T= 0K (Table S12). The similarity of the results indicate that FGR rates provide a reasonable description of the population dynamics.

Notice that calculations at 0K were performed also as a test, because they allow a more direct comparison with QD results. Fluorescence quantum yields were then obtained from FGR rates computed at 300K .

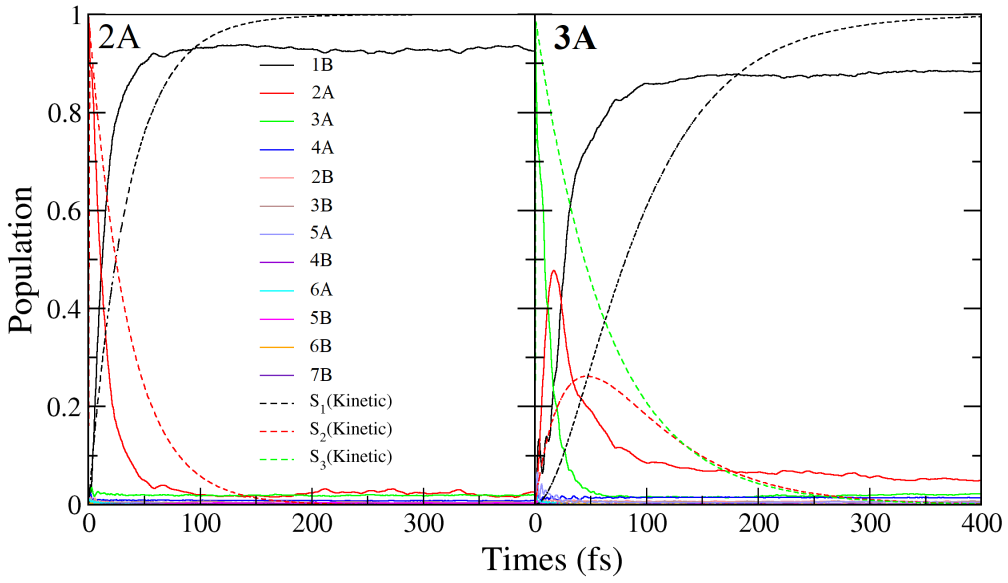

Figure S26: Comparison between quantum dynamics and kinetic model of electronic populations of aza[7]helicene in CH_2Cl_2, starting from S_2 and S_3.

Table S12: Internal conversion rates $k_{IC(ij)}$ obtained with Fermi Golden Rule at T = 0K. The rows indicate the initial state i which decay with constant $k_{IC(ij)}$ to the state in the column j.

	1	2	3	4	5	6	7	8	9	10	11	12
1	0	0	0	0	0	0	0	0	0	0	0	0
2	2.76E+13	0	2.58E+07	0	0	0	0	0	0	0	0	0
3	2.23E+11	1.57E+13	0	0	0	0	0	0	0	0	0	0
4	1.72E+10	4.39E+11	6.02E+12	0	4.82E+13	1.50E+10	4.44E+08	0	0	0	0	0
5	2.37E+10	5.27E+10	6.66E+12	7.26E+14	0	7.96E+11	3.02E+08	0	0	0	0	0
6	1.02E+10	1.57E+09	4.10E+12	4.38E+13	5.51E+14	0	1.04E+11	2.79E+08	6.86E+07	0	0	0
7	4.89E+06	9.89E+09	2.83E+11	3.19E+13	4.68E+12	1.40E+13	0	1.49E+10	1.95E+09	7.47E+09	0	0
8	3.28E+08	1.58E+09	3.85E+10	9.66E+11	6.37E+12	1.74E+13	3.05E+13	0	4.69E+13	5.72E+12	1.48E+10	7.85E+08
9	8.85E+05	1.40E+07	2.38E+10	8.51E+11	1.48E+12	2.52E+13	1.80E+13	9.15E+14	0	1.60E+14	2.32E+10	3.43E+09
10	2.54E+05	6.94E+08	2.25E+10	2.56E+12	3.30E+12	9.00E+12	1.54E+13	3.24E+12	3.84E+12	0	1.95E+09	1.54E+08
11	1.95E+07	2.85E+06	2.34E+10	6.53E+11	1.15E+11	1.97E+12	1.20E+13	1.06E+13	1.45E+13	6.09E+12	0	1.22E+12
12	1.44E+04	8.59E+05	2.40E+07	5.14E+08	3.34E+10	1.04E+12	1.93E+12	3.67E+13	3.07E+13	3.58E+13	1.03E+14	0

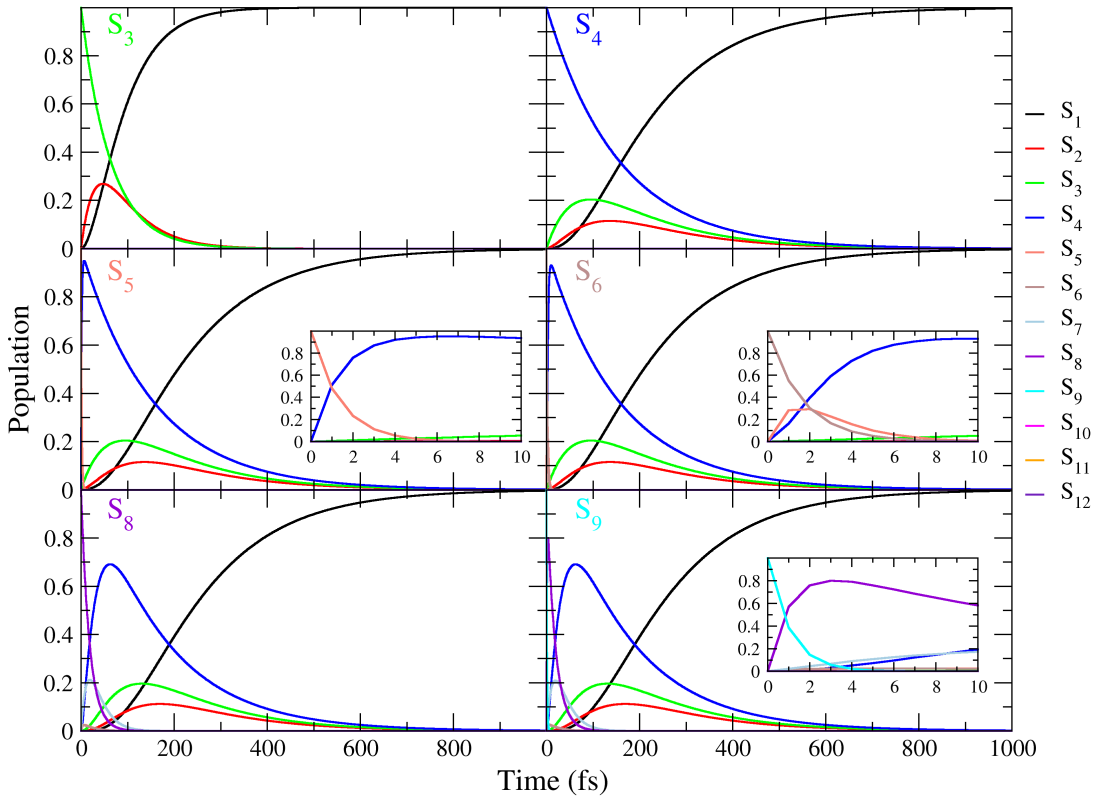

Figure S27: Time evolution of the populations P_i of the bright adiabatic states (oscillator strength >0.1) as predicted by the kinetic model based on k_{IC} rates computed with FGR. Initial conditions $P_i(0)$=1, $P_{j\neq i}(0)$=0, i=3,4,5,6,8,9. The insets show the first 10 fs.

S4.9 Additional Results on Triplets and Quantum Yield

A cartoon is shown in Figure S28, illustrating two possible analogies between a non-radiative decay (with coupling independent of the coordinates) and a radiative process (in Franck-Condon approximation) based on the fact that they are both described within FGR. The TD approach computes in one-shot the k_{nr} for a family of systems where the f PES is vertically displaced. The final expression can be interpreted as an absorption (Figure S28, panel a) for a system in which i and f have the same minimum energy and the searched value for our system is read at ΔE. Panel b (Figure S28), on the contrary, consider the i and f PES in the position they actually have in the system and show that the non-radiative decay is equivalent to an emission at ω=0 (so that energy is conserved). The two pictures are fully equivalent as it can be realized noticing that the rate is determined by the FC factors between the initial vibrational state and the final vibrational states highlighted by the green rectangle Figure S28), which are the same in both schemes.

Figure S29 shows the main transitions between Kohn-Sham molecular orbitals for the three lowest energy triplets. All the orbitals involve only π orbitals and there is no contribution from the n lone pairs of the nitrogen atoms. This reduces the effectiveness of the spin-orbit couplings, hindering the pathway to the triplets and favouring the radiative decay processes with respect to similar planar heterocycles, and can partially explain the high quantum yield (QY) reported for a helical molecule like aza[7]helicene.

Tables S13 and S14 report the most relevant parameters related to the decay processes and the calculated QY in gas phase and in solution with LR-PCM. These results are very similar to the SS-PCM presented in the main document. However, T_3 minimum is almost degenerated with S_1 if solvent effects are not/properly introduced in the model. Nevertheless, the QY in gas phase is also in perfect agree-

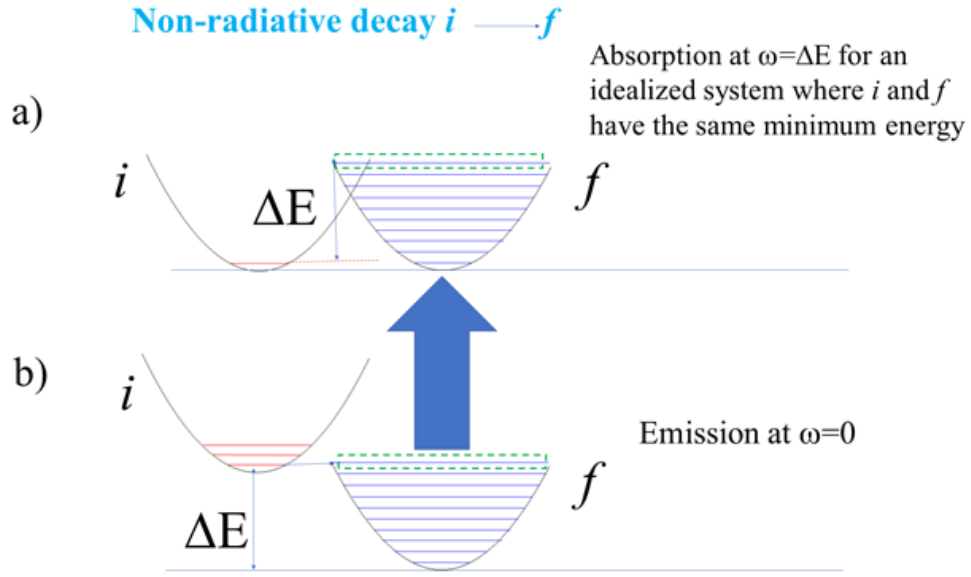

Figure S28: Two possible analogies between a non-radiative decay (with coupling independent of the coordinates) and a radiative process (in Franck-Condon approximation) based on the fact that they are both described within Fermi Golden Rule.

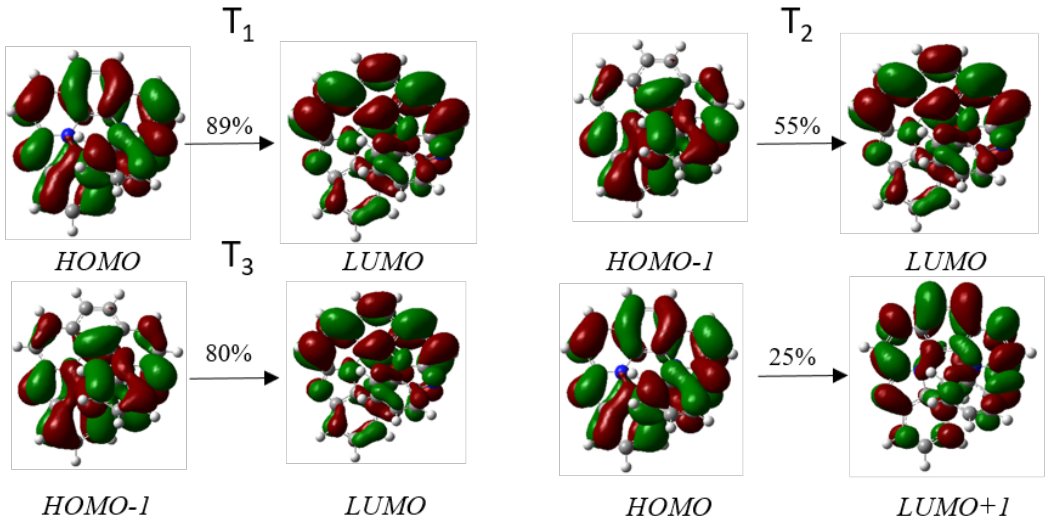

Figure S29: Molecular orbital transitions for the T_1, T_2 and T_3 excited states in S_1 minimum energy geometry. CAM-B3LYP/TZVP/PCM in equilibrium solvation.

ment with experiments ($QY^{gas} = 0.44$, $QY^{exp} = 0.39$) while with LR-PCM there are some deviations ($QY^{LR-PCM} = 0.62$), see Tables S15 and S16. These discrepancies with SS-PCM may be due to the smaller adiabatic energy obtained for T_3

Table S13: Excitation energies E_{gf} (eV) of the lowest excited singlet (S_i) and triplet (T_i) states, oscillator strengths δ_{OPA} for the S_0-S_i transition and molecular orbitals for S_0-T_i transition. Adiabatic energies (ΔE_{if}) are calculated with respect to S_1 in its minimum enegy structure, on which also the spin-orbit coupling constants (SOC) S_1-T_n and the intersystem crossing rate constant ($k_{isc}/10^7$) were computed for each of the four lowest energy triplets (T = 300K, HWHM = 0.06 eV). Data obtained in gas phase.

	S_i		T_i				
State	E_{gf}	δ_{OPA}	E_{gf}	Transition	ΔE_{if} (eV)	SOC (cm^{-1})	$k_{isc}/10^7$ (s^{-1})
1	2.70	0.16	1.39	H→L	0.90	0.26	0.01
2	3.35	0.00	2.27	H-1→L H→L+1	0.57	0.51	1.36
3	3.49	0.10	2.87	H-2→L H-1→L	0.07	0.41	4.17
4	4.20	0.04	3.07	H-3→L	0.04	0.54	0.09

in gas phase and specially in LR-PCM, which make the calculation more sensitive to numerical errors. Because in all cases T_3 carries the largest rate constant, the inaccuracies may have a larger impact. In fact, the lowest adiabatic energy is found for LR-PCM, which also shows the larger QY.

For the gas phase results, the possible contribution of the fourth triplet, T_4, was also considered. Its minimum is also slightly below S_1 one, even though in S_1 minimum it is about 0.37 eV higher in energy. Interestingly, the $S_1 \rightarrow T_4$ rate is remarkably slow with respect $S_1 \rightarrow T_2$ and $S_1 \rightarrow T_3$: two order of magnitude smaller. Therefore, T_4 plays no role on S_1 decay, and thus, it can be safely omitted for the calculations in solution.

The results in gas phase and in solution (LR-PCM) are also very robust to changes on the broadening of the Gaussian function, as shown in Tables S15 and S16: in gas phase the QY changes less than 0.02, while for LR-PCM is about 0.06.

Table S14: Excitation energies E_{gf} (eV) of the lowest excited singlet (S_i) and triplet (T_i) states, oscillator strengths δ_{OPA} for the S_0-S_i transition and molecular orbitals for S_0-T_i transition. Adiabatic energies (ΔE_{if}) are calculated with respect to S_1 in its minimum enegy structure, on which also the spin-orbit coupling constants (SOC) S_1-T_n and the intersystem crossing rate constant ($k_{isc}/10^7$) were computed for each of the three lowest energy triplets (T = 300K, HWHM = 0.06 eV). Data obtained in solution (LR-PCM).

	S_i		T_i				
State	E_{gf}	δ_{OPA}	E_{gf}	Transition	ΔE_{if} (eV)	SOC (cm^{-1})	$k_{isc}/10^7$ (s^{-1})
1	2.62	0.33	1.39	H→L	0.81	0.22	0.008
2	3.38	0.00	2.35	H-1→L H→L+1	0.42	0.45	1.78
3	3.50	0.46	2.87	H-2→L H-1→L	0.001	0.52	4.42

Table S15: Fluorescence quantum yields QY= $k_{rad}(\ k_{rad}+\ k_{ic}+k_{isc})^{-1}$ of aza[7]helicene, calculated with AH model. A Gaussian broadening function with different value of $HWHM_G$ was used, and the contribution of all the triplets is included in k_{isc}. T = 300K, calculations in gas phase. The QY estimate for SS-PCM is 0.38 ($HWHM_G$ = 0.06 eV).

$HWHM_G$ (eV)	$k_{rad}/10^7$ (s^{-1})	$k_{ic}/10^7$ (s^{-1})	$k_{isc}/10^7$ (s^{-1})	QY^{cal} ($QY^{exp} = 0.39$)
0.01	4.41	0.048	5.73	0.43
0.02	4.41	0.048	5.75	0.43
0.03	4.41	0.048	5.69	0.43
0.04	4.41	0.048	5.63	0.43
0.05	4.41	0.048	5.59	0.44
0.06	4.41	0.048	5.54	0.44

Table S16: Fluorescence quantum yields QY = $k_{rad}(\ k_{rad}+\ k_{ic}+k_{isc})^{-1}$ of aza[7]helicene, calculated with AH model. A Gaussian broadening function with different value of $HWHM_G$ was used, and the contribution of all the triplets is included in k_{isc}. T = 300K, calculations in solution (LR-PCM). For comparison, the QY estimate for SS-PCM is 0.38 ($HWHM_G$ = 0.06 eV).

$HWHM_G$ (eV)	$k_{rad}/10^7$ (s^{-1})	$k_{ic}/10^7$ (s^{-1})	$k_{isc}/10^7$ (s^{-1})	QY^{cal} ($QY^{exp} = 0.39$)
0.01	10.01	0.01	8.00	0.56
0.02	10.01	0.01	7.08	0.59
0.03	10.01	0.01	6.65	0.60
0.04	10.01	0.01	6.43	0.61
0.05	10.02	0.01	6.30	0.61
0.06	10.02	0.04	6.21	0.62

References

(S1) Aranda, D.; Santoro, F. Vibronic Spectra of π-Conjugated Systems with a Multitude of Coupled States. A Protocol Based on Linear Vibronic Coupling Models and Quantum Dynamics Tested on Hexahelicene. *J. Chem. Theory Comput.* **2021**, accepted, DOI: 10.1021/acs.jctc.1c00022.

(S2) Neugebauer, J.; Baerends, E. J.; Nooijen, M. Vibronic coupling and double excitations in linear response time-dependent density functional calculations: Dipole-allowed states of N 2. *J. Chem. Phys.* **2004**, *121*, 6155–6166.

(S3) Cimiraglia, R.; Malrieu, J.-P.; Persico, M.; Spiegelmann, F. Quasi-diabatic states and dynamical couplings from ab initio CI calculations: a new proposal. *J Phys B-at Mol Opt* **1985**, *18*, 3073.

(S4) Yaghoubi Jouybari, M.; Liu, Y.; Improta, R.; Santoro, F. The Ultrafast Dynamics of the Two Lowest Bright Excited States of Cytosine and 1-Methyl-Cytosine: A Quantum Dynamical Study. *J. Chem. Theory Comput.* **2020**, *16*, 5792–5808.

(S5) Neese, F. Software update: the ORCA program system, Version 4.1.1,WIREs Comput Mol Sci 2018, 8, e1327. doi: 10.1002/wcms.1327.

(S6) Hirata, S.; Head-Gordon, M. Time-dependent density functional theory within the Tamm–Dancoff approximation. *Chem. Phys. Lett.* **1999**, *314*, 291–299.

(S7) AbadGalán, L.; Castán, J. M.; ClémentDalinot,; SimónMarqués, P.; PhilippeBlanchard,; OlivierMaury,; ClémentCabanetos,; Bahers, T. L.; CyrilleMonnereau, Theoretical and experimental investigation on the intersystem crossing kinetics in benzothioxanthene imide luminophores, and

their dependence on substituent effects. *Phys. Chem. Chem. Phys.* **2020**, *22*, 12373–12381.

(S8) Schmidt, K. et al. Intersystem crossing processes in nonplanar aromatic heterocyclic molecules. *J. Phys. Chem. A* **2007**, *111*, 10490–10499.

(S9) Liu, Y.; Martínez Fernández, L.; Cerezo, J.; Prampolini, G.; Improta, R.; Santoro, F. Multistate Coupled Quantum Dynamics of Photoexcited Cytosine in Gas-Phase: Nonadiabatic Absorption Spectrum and Ultrafast Internal Conversions. *Chem. Phys.* **2018**, *55*, 452–463.

(S10) Liu, Y.; Xu, Q.; Jie, S.; Wang, L.; He, D.; Wang, M.; Yang, C. Insights for vibronic effects on spectral shapes of electronic circular dichroism and circularly polarized luminescence of aza[7]helicene. *Spectrochim. Acta, Part A* **2020**, *239*, 118475.

(S11) Otani, T.; Tsuyuki, A.; Iwachi, T.; Someya, S.; Tateno, K.; Kawai, H.; Saito, T.; Kanyiva, K. S.; Shibata, T. Facile Two-Step Synthesis of 1,10-Phenanthroline-Derived Polyaza[7]helicenes with High Fluorescence and CPL Efficiency. *Angew. Chem., Int. Ed. Engl.* **2017**, *56*, 3906–3910.

(S12) Nakai, Y.; Mori, T.; Inoue, Y. Theoretical and experimental studies on circular dichroism of carbo [n] helicenes. *J. Phys. Chem. A* **2012**, *116*, 7372–7385.

(S13) Nakai, Y.; Mori, T.; Sato, K.; Inoue, Y. Theoretical and experimental studies of circular dichroism of mono-and diazonia [6] helicenes. *J. Phys. Chem. A* **2013**, *117*, 5082–5092.

(S14) Frisch, M. J. et al. Gaussian˜09 Revision A.02. 2009; Gaussian Inc. Wallingford CT.

(S15) Frisch, M. J. et al. Gaussian˜16 Revision B.01. 2016; Gaussian Inc. Wallingford CT.

(S16) Santoro, F.; Lami, A.; Improta, R.; Bloino, J.; Barone, V. Effective method for the computation of optical spectra of large molecules at finite temperature including the Duschinsky and Herzberg–Teller effect: The Qx band of porphyrin as a case study. *J. Chem. Phys.* **2008**, *128*, 224311.